

Optical coherence tomography: A review

Nabila Eladawi^a, Mohammed Elmogy^a, Mohammed Ghazal^b,
Ali H. Mahmoud^a, Hatem Mahmoud^c, Marah Talal Alhalabi^b,
Ahmed Aboelfetouh^d, Alaa Riad^d, Robert Keynton^a, Shlomit Schaal^e,
Ayman El-Baz^a

^aBIOENGINEERING DEPARTMENT, UNIVERSITY OF LOUISVILLE, LOUISVILLE, KY, UNITED STATES ^bELECTRICAL AND COMPUTER ENGINEERING DEPARTMENT, ABU DHABI UNIVERSITY, ABU DHABI, UNITED ARAB EMIRATES ^cDEPARTMENT OF OPHTHALMOLOGY, FACULTY OF MEDICINE, AL-AZHAR UNIVERSITY, CAIRO, EGYPT ^dINFORMATION SYSTEMS DEPARTMENT, FACULTY OF COMPUTERS AND INFORMATION, MANSOURA UNIVERSITY, MANSOURA, EGYPT ^eDEPARTMENT OF OPHTHALMOLOGY AND VISUAL SCIENCES, UNIVERSITY OF MASSACHUSETTS MEDICAL SCHOOL, WORCESTER, MA, UNITED STATES

1 Introduction

Optical coherence tomography (OCT) is one of the fastest developing medical imaging modalities in the last decade. It can capture different aspects of biological tissues, such as blood flow, polarization status, structure data, elastic parameters, and molecular content [1]. Using OCT can give us an accurate knowledge of optical scattering and absorption of biological tissues. It helps in some diagnostic measurements, such as diagnosis of oral epithelial dysplasia, molecular diffusion in epithelial tissues, blood oxygenation measurement, blood glucose monitoring, plaque detection, and cancer detection [2, 3]. Therefore, OCT can be used to diagnose different diseases by analyzing the change in human tissues in the captured images.

OCT is considered as noninvasive, fast, and single-cell resolution imaging through several millimeters of the biological tissues. OCT is the same as ultrasound imaging except for reflections of near-infrared light that are detected rather than sound. It uses infrared light to give high-resolution three-dimensional (3D) insight into living tissues [4]. It is based on low-coherence interferometry to generate two-dimensional (2D) and 3D images. This principle obtains high-resolution, cross-sectional, and backscattering profiles [5]. Therefore, this imaging modality became popular due to ease of use, low cost, patient comfort, lack of ionizing radiation, and high resolution [6].

The first generation of OCT was time-domain OCT (TD-OCT). It encodes the location by time information about the position of a moving reference mirror to the location of the

reflection. It can acquire up to 400 A-scans (axial scan) per second. In 2001, the spectral-domain OCT (SD-OCT) was invented. It can acquire all the information in a single A-scan by evaluating the frequency spectrum of the interference between the reflected light and the reference mirror. SD-OCT is 40–110 times faster than TD-OCT. For example, swept source OCT is capable of acquiring 100,000 A-scans per second, which allows 3D data collection [7]. Recently, OCT has integrated with different imaging technologies, such as photoacoustics, multiphoton microscopy, fluorescent imaging, ultrasound, and adaptive optics, to overcome some of its limitations in order to enhance the performance [8].

OCT has been clinically used in ophthalmology [9, 10], cardiology [11, 12], endoscopy [13, 14], dermatology [15, 16], and oncology [15, 16]. In developmental biology, OCT has been used to characterize the morphological and functional development of organs, such as eyes [17], brain [18], limbs [19], reproductive organs [20], and heart [8, 11, 18, 21].

Moreover, OCT can be used for the analysis of skin surface topography especially with the existence of high-definition OCT (HD-OCT). HD-OCT provides a resolution of 3 μm in both axial and en-face planes. It has fast acquisition time (2–3 seconds) [22]. It provides noninvasive imaging of subsurface skin tissues for screening skin diseases, such as basal cell carcinoma and inflammatory diseases [23]. It can also be used for fingerprint acquisition as it is capable of providing high-resolution 3D scans of the fingerprint skin, which contains much information about the fingerprint [24]. In addition, OCT can help to understand some of the pathways influenced by the cardiac function in early heart development, such as the rapid beating and the complex ultrafine vasculature [8], coronary artery disease [25], and the structure of blood vessel wall in high details [26]. On the other hand, OCT can be used to study brain diseases, such as brain tumors [27] and stroke [28]. The high-resolution extension of OCT, optical coherence microscopy [29, 30], can achieve 1–2 μm resolution in tissue in all three dimensions. OCM can resolve individual neurons based on the intrinsic optical contrast in rodent brains [30–32] and human brain slices [33, 34].

As demonstrated in the literature, OCT shows promising results for diagnosing retinal diseases, which motivated us to focus on retina diseases in this short review. OCT can be considered as a standard modality for imaging the retina. Fig. 1 shows an example of OCT

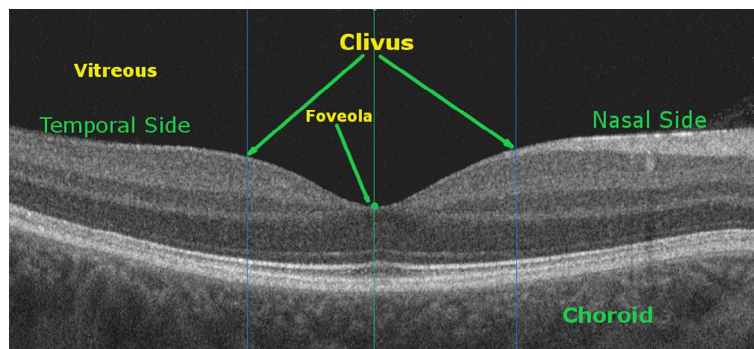


FIG. 1 OCT retinal image for a typical normal person in macular region of retina.

retinal image for a typical normal person. OCT is a noninvasive scan of the retina that shows its cross-sectional profile. In other words, OCT is a high-resolution cross-sectional image of the layers of the eye's biological tissues. It is used to visualize the retina to recognize and assess a variety of ocular diseases, such as diabetic macular edema (DME), glaucoma, and age-related macular degeneration (AMD) [35, 36]. The morphological features, such as the shape and distribution of drusen, cysts, macular holes (MHs), and blood vessels, can be easily visualized from OCT images and can be used as markers for diseases. Therefore, processing of OCT images becomes essential to do large-scale studies for changes in retina's layers. Many of the used techniques rely on the consistency of the OCT layer intensities to provide accurate results [6].

1.1 Retina anatomy in OCT

As it appears on OCT, the retina contains several layers with different thicknesses and intensities. Segmenting and measuring the thickness of each layer are considered as essential markers in assessing the health of the retina. The width and shape of individual layers may thicken or thin over the course of different diseases that indicate the current progress or status of a disease [6]. Irregularities in images can be used to diagnose many retinal diseases, such as AMD, retinitis pigmentosa, achromatopsia, glaucoma, and cone-rod dystrophy. The absence of certain layer(s) in the retina can be used as a marker for diagnosis, disease progression, and treatment monitoring [37].

Some studies preferred to define all intraretinal layer, whereas other studies preferred only to define the most critical retina layers that are needed to identify a disease. For example, Ishikawa et al. [38] defined four main layers, which are nerve fiber layer (NFL), ganglion cell layer (GCL) + inner plexiform layer (IPL), outer plexiform layer (OPL), and outer nuclear layer (ONL) + photoreceptor layer for healthy and glaucomatous eyes. Garvin et al. [39] detected five various layers from 3D OCT images for a patient with unilateral anterior ischemic optic neuropathy (AION) disease. These five layers were NFL, GCL + IPL, inner nuclear layer (INL) + OPL, photoreceptor inner segments (PIS), and photoreceptor outer segments (POS).

Bagci et al. [40] were able to detect six different retinal layers, which are NFL, IPL + GCL, INL, OPL, ONL + PIS, and POS from normal healthy eyes. Lu et al. [41] identified and measured the thickness of six layers extracted from 3D images of healthy subjects. These layers were NFL, PIS, POS, retinal ganglion cell (RGC), IPL, and OPL. Rossant et al. [42] detected eight layers from healthy subjects. Yang et al. [43] detected nine boundaries from 3D images of healthy and glaucomatous eyes.

Shi et al. [35] were able to segment 10 retinal layers in 3D images of patients with retinal pigment epithelial detachments (PED). Sugrk et al. [36] proposed a segmentation method to find the retinal pigment epithelium (RPE) layer and to detect a shape of drusen in this layer. Then, the RPE layer is used to find retinal nerve fiber layer (RFL) and to detect a bubble of blood area in RFL complex. ElTanboly et al. [44] detected 12 different layers, which are NFL, GCL, IPL, INL, OPL, ONL, external limiting membrane (ELM), myoid zone (MZ),

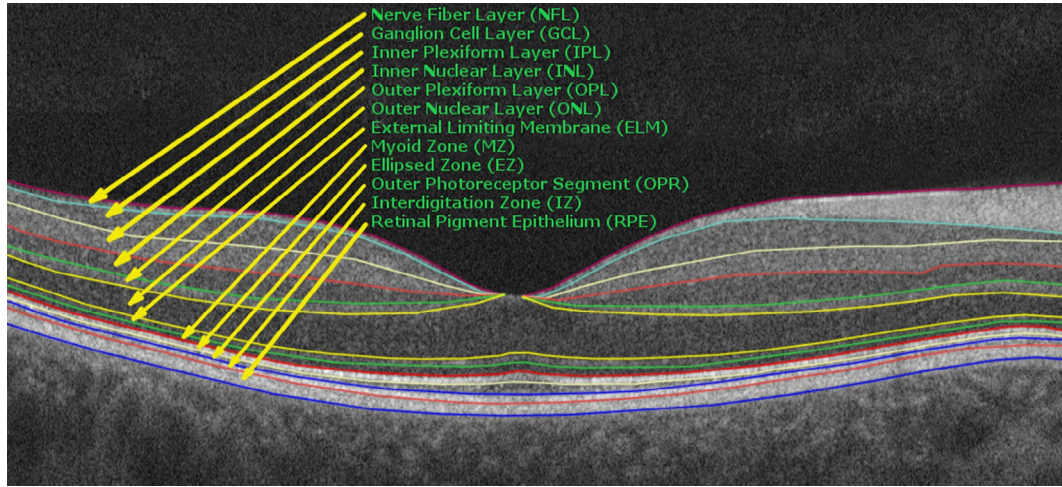


FIG. 2 OCT retinal image with its distinctive 12 layers for a typical healthy person in macular region of retina.

ellipsoid zone (EZ), outer photoreceptor (ORP), interdigitating zone (IZ), and RPE layers. Fig. 2 shows an OCT retinal image with its 12 distinctive layers for a typical healthy person.

The focus of this survey is to discuss the current findings in OCT retina images with respect to the effect of different diseases on the retina layers. We will discuss the current studies for each disease and how it affects the structure of the various layers in OCT images. We will concentrate on the methodologies of handling different OCT images for normal and diseased retinas. Then, we will discuss the current challenges and research topics in this field.

2 Related work

As previously mentioned, OCT images can be used to show the structure of the retina. The detected layers in the OCT retinal images can be utilized as an indicator for healthy and diseased eyes. Recently, there are many studies, which are conducted to analyze the OCT retinal images to classify the healthy from diseased patients. Each disease can be classified depending on some characteristics that can be absent or found in the OCT images. In the following sections, we will discuss the current work in normal eyes as well as the diseased eyes. We will begin with the detection of the retina's layers in healthy persons. Then, we will discuss the characteristics and studies of the most common diseases, which can be indicated by the analysis of the OCT retinal images.

2.1 Normal healthy eye

As OCT has histological correspondence, the interpretation of the OCT image seems to be quite intuitive. However, OCT technology depicts tissue reflectivity. It is dependent on the

tissue optical properties, that is, microscopic variations in the refractive index of subcellular structures, and on the amount of light signal that the tissues absorb [45, 46]. When analyzing an OCT image for retina, there is no standard for the number of layers. Most studies estimate 4, 7, 10, 11, or 12 layers. On the other hand, normal retinal thickness differs from one device to another due to different characteristics, such as age, gender, race, and refraction. In addition, all measurements using SD-OCT have higher values than using TD-OCT due to the higher resolution [47].

Bagci et al. [40] detected six different layers (NFL, IPL + GCL, INL, OPL, ONL + PIS, and POS) in OCT retinal images. They proposed an algorithm that was able to segment retinal layers. This algorithm is developed based on 2D edge detection scheme that suppresses speckle noise and at the same time enhances the edges along the retinal depth. A gray-level mapping technique was proposed to overcome uneven tissue reflectivity and variance across subjects. Their system was tested only on normal subjects. The tested images were taken by two different OCT devices. First, images of 15 normal subjects were taken using the Stratus OCT device with the average of their ages was 57 ± 11 years old. Second, images of 11 normal subjects were taken using RTVue OCT device with average age equals to 56 ± 7 years old. The thickness of all the layers was measured and compared with the results of three manual observers. The mean absolute values were between 3 and $4\mu\text{m}$ for both automated and manual thickness measurements. Additional work is needed to prove the ability of this proposed system to deal with images that are obtained from patients with different retinal diseases.

Rossant et al. [42] determined eight layers (RNFL, ONL, GCL + IPL, INL, OPL, IS, OS, and RPE) in high-resolution OCT images. They proposed a segmentation method for detecting the layers by using the knowledge about the relative position of the layers. The system used 25 normal subjects with 72 images. In all, 14 images were chosen to be manually segmented by five experts. They calculated the distance between the manually traced curves and the ones obtained by the proposed method. The measures that are manually performed by the experts and those obtained from the automatic segmentation were very close. This algorithm was tested only on normal eyes. In addition, it lacked more details about the evaluation of the proposed technique. They noticed a change in the profile of the fovea with the axial length. When the central ONL thickness increased, the foveal thickness increased. A significant variability of the OPL/ONL complex was noted independently of axial length. The maximal retinal thickness was stable over a large range of axial length and had a low coefficient of variation. Finally, no differences that are related to gender were noted.

Lu et al. [41] detected and measured the thickness of six different layers (RNFL, IS, OS, RGC, IPL, and OPL) in OCT retinal images. The proposed segmentation algorithm cuts the OCT image into the vessel and nonvessel sections. First, the vessel section is detected by the polynomial smoothing procedure. Then, the nonvessel section was filtered using two filters, which were bilateral and median filters. The layers were then detected and classified. For the layers in the vessel section, they were defined using linear interpolation of the layer boundaries that were detected in the nonvessel section. The system was tested using

the images of four healthy subjects. There was more error in the thickness measure at the vessel section. Errors varied due to different image noise level and layer boundary quality. Errors were occurred more often in measuring the thickness of RNFL. The algorithm measured it thicker than it should be. This algorithm needs advanced image interpolation techniques to improve the layer boundaries of the vessel sections. In addition, it requires other advanced image smoothing techniques, which are important to be able to segment non-RNFL layers that are often much thinner than the RNFL. The algorithm needs to be evaluated over a larger dataset.

Kajic et al. [4] detected and built the thickness maps for eight intraretinal layers in normal eyes. First, they learned the variation parameters from the training data that were manually segmented. Then, these parameters were used to drive a model to able to segment unseen data. The algorithm was evaluated against a large set of images that were manually segmented. In all, 466 images from 17 eyes were manually segmented twice by two different persons using Amazon Mechanical Turk workers. This algorithm could produce accurate results even in the existence of strong speckle noise. It showed only a larger variation around the foveal region. Even when they added background noise to the images, the algorithm showed robust performance. On the other hand, further investigation is needed to test the proposed algorithm on patient subjects.

Salarian et al. [48] proposed a method to detect certain layers using graph theory and the shortest path algorithm. They chose the regions of interest that could be used in normal cases and some abnormal ones. They discovered that by changing some parts, such as ILM, RNFL, and RPE, these layers could be found easily. They applied the proposed technique to all B-scan images of 16 people, including low-quality images and some images with diseased eyes. The results were accurate based on the manual segmentation of an expert. In the future, they can apply other ways of weighting or use other types of information to improve the proposed method. This modification can be useful for savior diseased cases.

Lang et al. [6] adapted the N3 framework that was originally implemented to correct MRI data for intensity inhomogeneity correction in OCT images. To create a template intensity profile for each layer, they transformed the data to a flattened macular space, which afforded an accurate initial estimate of the gain field. To correct the data, N3 produced a smoothly varying field. Their proposed methodology was capable of both recovering synthetically generated gain fields and improving the stability of the layer intensities. They made manual segmentation for 41 OCT images. They delineated nine boundaries on every B-scans.

2.2 Glaucoma

Glaucoma is a set of neurodegenerative eye diseases that leads to the loss of vision and blindness. It is the second leading cause of blindness in the world [49]. Both NFL thickness and the Euclidian distance between NFL and the inner limiting membrane (ILM) can be used as markers for the glaucoma disease. The glaucoma patient has a decreased NFL

thickness as compared to the typical healthy subjects. Recently, it has been said that both of the choroid thickness and a measure of separation between Bruch's membrane (BM) and choroid can also be used as a marker of the glaucoma disease [50].

Many studies have been made to diagnose the glaucoma disease depending on the OCT retinal images. For example, Ishikawa et al. [38] detected four various layers (macular nerve fiber layer [mNFL], inner retinal complex [IRC], OPL, and outer retinal complex [ORC]) in OCT retinal images. They applied an adaptive thresholding technique to search for borders of retinal layer structures on each sampling line. They tested their system on normal and glaucomatous subjects. They used 16 subjects for training (5 normal and 11 affected by glaucoma disease) to assess their proposed system. The average ages for normal and diseased subjects were 52.1 ± 14.8 and 62.4 ± 14.5 years old, respectively. On the other hand, they used 64 subjects for testing their proposed system (27 normal and 37 glaucomatous). The algorithm failed to detect the layers with 55.6% in poor quality images and failed with 10.2% in good quality ones. The ILM layer was the most reliable board, while the IRC layer was the least reliable one. From the experimental results, they found that in normal subjects the mFNL, IRC, total retinal thickness, and cpNFL were thicker. The best-performing macular segmentation parameter in this study was mNFL IRC thickness. To improve the overall performance of this system, they need to use better methods and procedures for preprocessing, filtering, and border detection.

Yang et al. [43] detected the boundaries between some retinal layers by proposing an automated boundary segmentation algorithm for 3D OCT images. First, a customized Canny edge detection was used to create a map that showed main local edges. Then, a graph was built based on the axial intensity and the Canny edge map. Finally, the layers were extracted using the shortest path search through the graph. The algorithm was able to define nine different boundaries. These boundaries were the ILM boundary, the boundary between NFL and GCL, the one between GCL and IPL, the one between IPL and INL, the one between INL and OPL, the ELM boundary, the one between IS and OS, the one between OS and RPE, and the one between BM and choroid. The algorithm was tested on 19 healthy subjects and 19 with glaucoma disease. The results were compared with the results from four manual segmentation experts. The difference between the measurement of ILM, INL/OPL, and BM/choroid boundaries versus the manual segmentation was very close to the different between segmenters. The NFL/GCL and IPL/INL versus the manual segmenters were larger than between segmenters but when the fovea area was excluded the difference was improved. The problem in the NFL/GCL boundary was on the side, where NFL is thin. It was detectable, but it was detected thicker. This algorithm, even in the poor quality image (low intensity and low contrast) still able to detect the boundary. The algorithm notices that the NFL was clearly thinner in the glaucoma patients.

Varmeer et al. [51] worked on 3D images to detect six retinal layers (vitreous, RNFL, GCL + IPL, INL + OPL, photoreceptor + RPE, and choroid). The proposed system worked well for both normal and diseased eyes with glaucoma. It was able to build the thickness maps for single or combined layers. The algorithm used 10 healthy subjects and eight subjects with glaucoma. Two scans held manually for the healthy ones, and one scan for the

diseased one. RMS errors were between 4 and 6 μm for the top and bottom of the retina. The errors for intraretinal interfaces were between 6 and 15 μm . The resulting total retinal thickness maps corresponded with known retinal morphology. They compared RNFL thickness maps with GDx (Carl Zeiss Meditec) thickness maps, and both were mostly consistent. In OCT-derived thickness maps, local defects, which are found in temporo-superior and temporo-inferior regions, were better visualized. In the two cases of glaucoma, the RNFL is thinner than in the normal eye.

Kafieh et al. [5] introduced a segmentation technique based on a variant of spectral graph theory, which was called diffusion maps. It relied on regional image texture in localizing boundaries in situations of low image contrast and poor layer-to-layer image gradients. Their proposed method was based on the application of two sequential diffusion maps. The first one segmented the ILM-to-RPE. The second one localized the internal layers between the ILM and the RPE complexes. To partition the data into important and less important sections and to localize the internal layer. They applied this method to 2D and 3D OCT datasets. In experimental results, they tested the proposed technique on 23 images dataset from two groups (normal and glaucoma patients). The mean unsigned border positioning errors (mean \pm SD) was $8.52 \pm 3.13 \mu\text{m}$ for a 2D method and was $7.56 \pm 2.95 \mu\text{m}$ for a 3D method.

Bogunovic et al. [52] proposed an algorithm to segment intraretinal layers of OCT images. After 2D en-face alignment, all the fields were segmented simultaneously. To penalize deviations from the expected surface height differences for each pair of overlapping fields, they imposed a priori soft interfield-entrasurface constraints. They were extracted to be the depth-axis shifts, which produced the maximum cross-correlation of pairwise-overlapped areas. The algorithm could segment 11 surfaces, but the evaluation was focused on only four surfaces to the ease of manual tracing. These surfaces are ILM, the surface between NFL and GCL, the surface between IPL and INL, and the outer boundary of RPE. These four surfaces enabled the algorithm to compute the thickness of NFL, GCL + IPL, and total retinal thickness. The method was evaluated using 180 images acquired from 10 glaucoma patients (3 severe, 5 moderates, and 2 mild). The obtained average error was $4.58 \pm 1.46 \mu\text{m}$, which was comparable to the average difference between different observers $5.86 \pm 1.72 \mu\text{m}$. The overall mean thickness per patient was $1.07 \pm 0.35 \mu\text{m}$ for NFL, $0.73 \pm 0.31 \mu\text{m}$ for GCL + IPL, and $1.86 \pm 0.35 \mu\text{m}$ for total retinal.

2.3 Central serous chorioretinopathy

Central serous chorioretinopathy (CSC) is a chorioretinal illness, which is not understood completely with systemic associations. It has a multifactorial etiology with a very complicated pathogenesis. Ophthalmoscopic indications of CSC range from mono- or paucifocal RPE lesions with a noticeable increase of the neurosensory retina by clear fluid (regular in the recent onset cases) to shallow detachments overlying large patches of irregularly depigmented RPE. Because of the fluid that is accumulated under the retina distortions

or visual loss may appear. In normal and CSC diseased subjects, the 3D configuration of the subretinal fluid differs [53]. So, detecting these changes in both of fluid and RPE can help in diagnosing this disease.

Some studies were done to diagnose the CSC patients by analyzing the OCT retinal images. For example, Eandi et al. [54] determined the foveal thickness and anatomical changes in the fovea and visual acuity in unilateral resolved CSC patients. In this study, 20 patients were involved with an age range between 31–66 years old. They normalized the foveal thickness by dividing its value by the uninvolved fellow eye value. The best-corrected visual acuity was normalized also. Patients with unilateral resolved CSC had a decreased central foveal thickness. Therefore, there was a correlation between this thickness and the visual acuity. In addition, there was the inability to observe the ELM layer in most of the diseased eyes. There was also difficulty in observing the boundary between the photoreceptor bodies and the outer segments. All these observations were correlated with visual acuity.

Imamura et al. [55] evaluated the choroidal thickness in patients with CSC disease. The thickness of the subfoveal choroidal was measured from the inner scleral border to the outer border of the RPE. In this study, 19 patients with 28 eyes were involved. The mean age of them was 59.3. The measured choroidal thickness was $505 \pm 124 \mu\text{m}$, which was much greater than the choroidal thickness in normal eyes ($P < .001$).

Novosel et al. [56] presented a locally adaptive approach based on loosely coupled level sets to segment the fluid and the interfaces between retinal layers in eyes affected by CSR. The approach exploited the local attenuation coefficient differences of layers around an interface. To delineate the fluid, the approach introduced auxiliary interfaces. The approach could handle abrupt attenuation coefficient variations and topology disrupting anomalies. The mean absolute deviation for the interfaces was $3.7\text{--}8.9 \mu\text{m}$ (1–2 pixels), and the Dice coefficient for the fluid segmentation was 0.96 compared to a manual segmentation. They segmented the retinal layers and fluids simultaneously. So, they aided each other in retrieving the right segmentation. An error of $3.9 \mu\text{m}$ corresponded to 1 pixel along the A-lines. The accuracy showed an RMSE ranging from 4.4 to $13.4 \mu\text{m}$ and a MAD ranging from 3.7 to $8.9 \mu\text{m}$. The Dice coefficient, TPR, and FPR were 0.96, 95%, and 1%, respectively.

2.4 Anterior ischemic optical neuropathy

AION is causing damage to the optic nerve from inadequate blood supply that results in loss of vision. There are two main types of AION: arteritic AION (AAION) and nonarteritic AION (NAION or AION). In NAION, the retinal NFL layer thickness is significantly increased in the acute stage. Then, it is significantly decreased in the resolving stage. In the sequent paragraphs, some of the current work concerning both types of the AION diseases is discussed. Fig. 3 shows a NAION case captured by ZEISS OCT machine.

Garvin et al. [57] detected five layers (NFL, GCL + IPL, INL + OPL, IS, and OS) in OCT retinal images. The layers were identified by finding a minimum-cost closed set in a

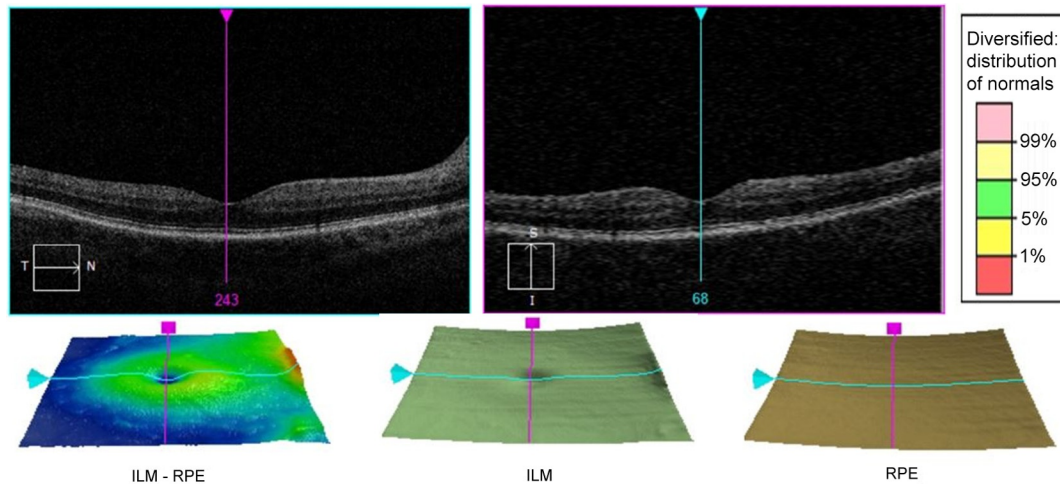


FIG. 3 A NAION case captured by ZEISS OCT machine.

constructed geometric graph. This graph is constructed from the edge/regional information and a priori determined surface smoothness and interaction constraints. This study was conducted on 3D images for 12 patients with AION disease for one eye or both. They observed that there were changes in both the inner and the outer retinal thickness for the affected eye. The inner retinal thickness was $24.1 \mu\text{m}$ smaller than unaffected one, and the outer retinal thickness was $3.7 \mu\text{m}$ smaller in the affected eye. The results were compared with the results of three manual observers. The border positioning errors and thickness differences between the observers were very close to those of the results and the reference standard. Their algorithm attempted to segment all surfaces although sometimes some layers are not present. In some images, surface two might not be visible, and some images were too noisy to resolve the layer boundaries.

Garvin et al. [39] provided two extensions of their previous work. The first extension was the ability to incorporate varying feasibility constraints and capacity to incorporate true regional information. The second was that they applied a new method on retinal layers in SD-OCT images. Therefore, their proposed method extracted seven surfaces from the processed images. In addition, they found that the bigger coverage of the macular region generated a greater variation of layer appearances.

Hedges et al. [58] demonstrated the existence of subfoveal fluid, which was associated with optic disc swelling from NAION. In this study, 76 patients were involved. Eight patients had apparent subretinal fluid that extended into the subfoveal space. The visual acuity was improved in five of these eight patients as the subfoveal fluid resolved. However, they concluded that the subretinal fluid was developed in some patients with NAION. In addition, they found that this disease might cause visual acuity loss.

2.5 Diabetic macular edema

DME can cause vision loss in persons with diabetes mellitus. It can be defined as a blood leakage pass in RPE layer and photoreceptor inner/outer segment (IS/OS) from choroid into the RNFL complex. The visual ability is lost by increasing the area of the blood or bubble that is found in the RNFL complex. In the United States, there are approximately 26 million persons suffering from DME [36, 59]. OCT modality is used to find the presence of the blood area or bubble in the RNFL complex. In addition, the diagnosis of the DME can be made by measuring the variation of the thickness in some retinal layers. Fig. 4 shows an OCT retinal images for a DME patient.

Due to fluid accumulation that can be intracellular or extracellular, DME increases the retinal thickness. Due to the increased fluid intake, the cells are enlarged in intracellular edema. Otherwise, extracellular edema results from fluid accumulation outside the cell. In the second type of edema, hard exudates can be structured because of the lipid contents of the leakage can agglomerate into an irregular shape. Finally, each eye of a DME patient can present regions with different characteristics, such as increased ONL thickness, cysts, and even areas without any visible changes [60].

Current studies have shown that the visual acuity can be predicted by the volume of retinal tissue within fluid-filled spaces [61]. Further, clinical studies based on the volume of cystoid fluid and the location of the cysts may be used as a metric for visual prognosis. In addition, the presence of diabetic cysts may alter the normal pattern of the subretinal layers leading to subretinal disorganization. The extent of disorganization can be estimated using a method of localizing these cysts in certain subretinal layers [49].

Roychowdhury et al. [62] localized cysts in OCT images for patients with DME. In each image, six subretinal layers were identified using an iterative high-pass filtering approach.

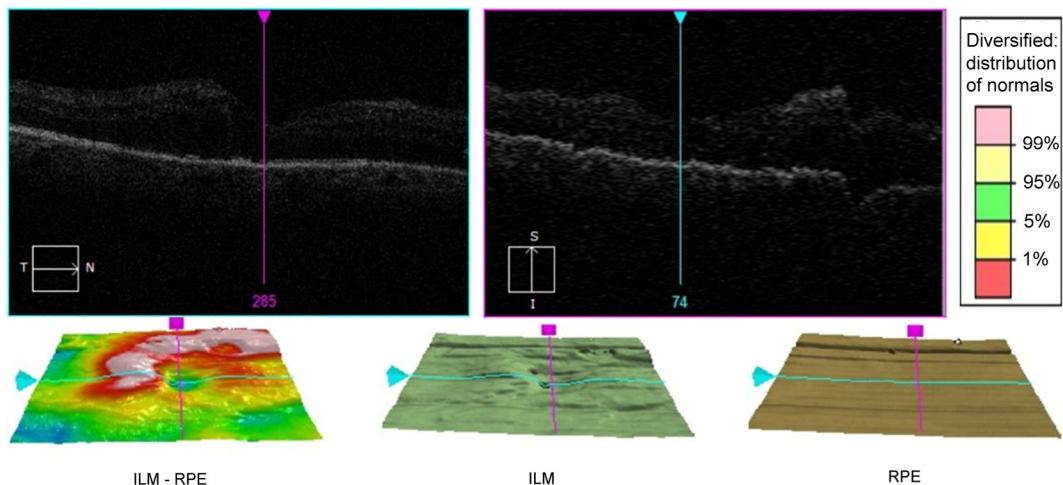


FIG. 4 A DME case captured by ZEISS OCT machine.

Then, dark regions were detected as candidate cystoid regions. To estimate the area of cystoid regions, each candidate cystoid region was analyzed using solidity, mean, and the maximum pixel value of the negative OCT image as decisive features. This algorithm was capable of determining the boundaries of contiguous cysts by breaking down large cysts. This system was able to detect cystoid area with 4.6% mean and 6.6% standard deviation based on 120 OCT images of 25 DME patients. This method achieved 100% sensitivity and 75% specificity in separating images with no cysts from the ones with cysts. In addition, it achieved 90% correlation between the manually segmented area and the cystoid area defined by the algorithm. This algorithm located the cysts in the inner plexiform with an accuracy of 88%, in inner nuclear with an accuracy of 86%, and in outer nuclear regions with an accuracy of 80%.

Roychowdhury et al. [49] produced 3D thickness maps for images of normal subjects and patients with DME. The first stage of the proposed algorithm was to make de-noising for OCT images. Then, they applied the automated segmentation method to extract the layers using multiresolution high-pass filtering. They extracted only six retinal layers (NFL + IPL, INL, ONL, inner layer, and outer layer) with their thickness from all the tested images to form the thickness maps. They applied this system to 203 normal images from 10 healthy subjects and 357 images from 15 patients with DME. They measured the correlation coefficient (r) between the results of the proposed system and the manual segmentation. They obtained $r > 0.8$ in normal cases and $r > 0.7$ in abnormal ones. They found that the thickness of the inner layer with DMA was 1.12 times more than normal cases. In DME cases, the INL layer appeared relatively thicker, and the ONL layer appears irregular and exceeding 200 μm . Therefore, the thickness maps of the INL and ONL could be used as an indicator of disease severity and for tracking the changes in DME patients overtime.

Correia et al. [60] identified the changes happened to ONL layer in DME patients. The OCT images were obtained from healthy subjects as controls and patients with DME. The images were distributed into three groups. These groups were healthy subjects, DME patients where ONL thickness was significantly increased, and DME patients with normal thickness for ONL. For all processed images, the ONL was segmented and processed to produce a representative A-scan. They used the optical and physical characteristics of the healthy human retina as a reference in their proposed system. They used a Monte Carlo technique with a model for the ONL to simulate an A-scan for each group and compare it to the real OCT data. The results showed that there were two types of edema, cytotoxic (intracellular) and vasogenic (extracellular). In the DME without changes in the ONL group, the most observed feature for the real OCT data was the increase in the volume of the nucleus. The data of patients with DME with increased ONL could be created by increasing ONL thickness from the healthy status by the exact increase in ONL thickness.

Abhishek et al. [63] segmented the intraretinal layers for edema patients and normal subjects. The segmented layers were ILM and RPE layers. The graph-based segmentation was solely based on the pixel intensity variation and distance between neighbor pixels. They used the weighting scheme and shortest path search to identify the neighborhood pixel. In this algorithm, the preprocessing step could be considered as optional.

There were 12 diseased images and 9 normal images. The algorithm was able to detect ILM and RPE layers in 7 out of 9 normal subjects and 11 out of 12 DME affected subjects due to expert validation. It was found that the range of the thickness of the normal subject was less than 50, whereas the range of the DME subjects was more than 50. In some cases, it even reached 200. So, the thickness could be used as a good sign of the presence of edema. In this method, if they limit the search regions it can detect the other retinal layers. Another advantage of this method is that it is less prone to noise.

2.6 Cystoids macular edema

Cystoids macular edema (CME) occurs in a variety of diseases like diabetic retinopathy, AMD, retinal vein occlusion, and intraocular inflammation [64]. It affects the full thickness of the retinal tissue involving the anatomic fovea [65]. It appears more often in people over 60 years old. It affects visual acuity and may lead to loss of vision or even blindness.

There are some current studies that discuss the diagnosis of CME disease from analyzing the OCT retinal images. For example, Zhang et al. [66] determined the volume of CME for the retinas with MH in 3D OCT images. Their system consisted of three main phases, which were preprocessing, coarse segmentation, and fine segmentation. The preprocessing phase included denoising, intraretinal layers segmentation and flattening, and MH and vessel silhouettes elimination. An AdaBoost classifier was used to get the seeds and constrained regions for graph cut in the second phase. In the last phase, a graph cut algorithm is used to get fine segmentation results. The proposed system was evaluated by 3D OCT images from 18 patients with CMEs and MH. The true positive volume fraction (TPVF) was 84.6%, and the false positive volume fraction (FPVF) was 1.7%. The accuracy rate (ACC) for CME volume segmentation was 99.7%. For the validation, a leave-one-out strategy was used during training and testing. Supervised by an experienced ophthalmologist, the CME regions were segmented manually to work as ground truth. However, a more accurate shape model of the MH (includes the maximum/minimum diameter of the MH) was needed. In addition, the proposed system detected the obvious cyst only.

Slokom et al. [67] identified CME regions in SD-OCT of the macula. An algorithm was made to detect cystoids. First, it identified the borders of the cystoids. Then, to obtain surface area of fluid in the image, a quantitative analysis of liquid in cystoids regions was made. They used data from six patients with CME associated with diverse retinopathy. In the central part of the retina, two patients had a singular cystoids region, and the others had multiple cystoids regions. They applied the distribution metric for image segmentation that appeared as a result from prediction theory to detect cystoids in OCT images. Applying level set process, an energy model based on the metric was incorporated into the geometric active contour algorithm. The clinical expert classified the extracted results from every image as good and fair extraction. In all, 95% were classified as good and fair extraction cases. The average precision was 95.02% and average sensitivity was 88.46%. The area of each cystoids region was calculated and compared to the manual extraction, which was in all cases smaller than those of the clinical expert.

2.7 Age-related macular degeneration

In the United States, there are approximately 8 million persons who have monocular and binocular AMDs. This disease is detected by searching for drusen, which is defined as abnormality between the basal lamina of RPE and the inner collagenous layer of BM [68, 69]. Fig. 5 shows an OCT retinal image for AMD patient.

Khanifar et al. [70] categorized the drusen ultrastructure in AMD using OCT retinal images. A sample of 31 eyes of 31 AMD patients was utilized in this study. The images were analyzed, and the drusen were scored by four categories, which are shape, predominant internal reflectivity, homogeneity, and the presence of overlying hyperreflective foci. They calculated the spread of each morphologic pattern and the combinations of the extracted morphologic patterns. In all, 21 images were chosen for the adequate quality. In all, 17 drusen were found from 120 drusen in the whole images. Most of the found drusen were convex, homogeneous, with medium internal reflectivity, and without overlying hyperreflective foci. Nonhomogenous drusen were found in 16 eyes, 5 of them have a distinct hyperreflective core. Hyperreflective foci overlying drusen were in seven eyes.

Schuman et al. [71] detected the changes in the retina using OCT images in AMD patients. In all, 17 eyes of 12 patients with nonneovascular AMD and drusen were used. In all, 17 eyes of 10 age-matched were used as a control. Over 97% of drusen, the PRL was thinned. The average PRL thickness was reduced by 27.5% over drusen. They found that difference was valid and significant ($P = .004$). They observed two types of hyperreflective abnormalities over drusen in the neurosensory retina. Finally, they concluded that distinct hyperreflective speckled patterns occur over drusen in 41% of AMD eyes and never in control eyes.

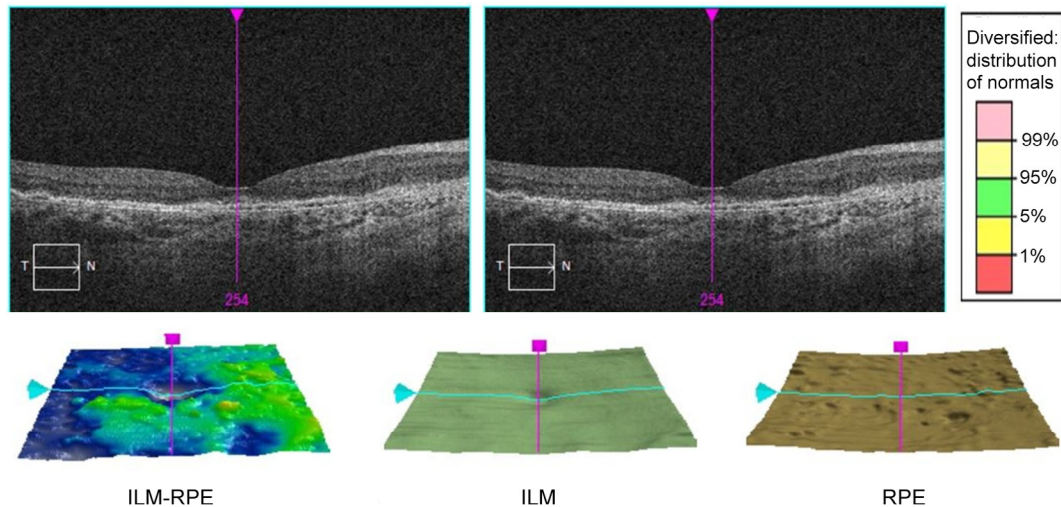


FIG. 5 An AMD case captured by ZEISS OCT machine.

Oliveira et al. [72] proposed a method to integrate sparse higher-order potentials (SHOPs) into a multisurface segmentation framework. It was used to confront with local boundary variations caused by drusen, which was important to evaluate AMD progress. The mean unsigned error for the inner retinal pigment epithelium (IRPE) was $5.65 \pm 6.26 \mu\text{m}$ and for BM was $4.37 \pm 5.25 \mu\text{m}$. The results were comparable to those obtained by two experts. Their average interobserver variability was $7.30 \pm 6.87 \mu\text{m}$ for IRPE and $5.03 \pm 4.37 \mu\text{m}$ for BM. The IRPE and the other boundaries were successfully segmented. Their proposed technique was evaluated in a dataset of 20 AMD patients. The dataset also included manual segmentations of the ILM, IRPE, and BM boundaries performed by two expert graders.

2.8 Other different diseases

In this section, we discuss other work that does not lay under any of the above diseases or research studies that deal with more than one disease. First, we discuss the PED, which is considered as a notable feature of many chorioretinal disease processes, including AMD, polypoidal choroidal vasculopathy, CSC, and uveitis. It can be classified as serous, fibrovascular, or drusenoid.

Shi et al. [35] proposed a framework for segmenting the retinal layers in 3D OCT images with serous retinal PED. Their framework consisted of three main stages. The first stage was the fast denoising and B-scan alignment. The second stage was the multiresolution graph search-based surface detection. Finally, the third stage was the PED region detection and surface correction above the PED region. They evaluated their system by using 20 PED patient. The experimental results showed that the TPVF was 87.1%, the FPVF was 0.37%, the positive predicative value for PED was 81.2%, and the average running time was 220 seconds for OCT data of $512 \times 64 \times 480$ voxels.

On the other hand, Sugmuk et al. [36] proposed a segmentation technique to divide OCT images to detect the shape of the drusen in the RPE layer. They used the RPE layer to find RFL layer to detect a bubble in the blood area. They used binary classification technique to classify AMD and DME diseases depending on the retrieved characteristics. They used only 16 OCT images (10 images for AMD and 6 images for DME) in their experiments. Their proposed classification system achieved 87.5% for accuracy.

ElTanboly et al. [73] proposed a segmentation framework for retinal layers from 2D OCT data. Their framework was based on the joint model, which included shape, intensity, and spatial information. It could segment 12 distinct retinal layers in normal and diseased subjects. The shape was built using a subset of coaligned training OCT images, which were initially aligned using an innovative method to employ multiresolution edge tracking. Then, the visual appearance features were described using pixel-wise image intensities and spatial interaction features. A linear combination of discrete Gaussians was used to model the empirical gray-level distribution of OCT data. To eliminate the noise, they integrated the proposed model with a second-order Markov-Gibbs random field spatial interaction model. They tested their framework on 250 normal and diseased OCT images with AMD and DR. Their proposed segmentation method was evaluated using Dice coefficient

($DSC = 0.763 \pm 0.1598$), agreement coefficient ($AC1 = 73.2 \pm 4.46\%$), and average deviation distance ($AD = 6.87 \pm 2.78 \mu\text{m}$) metrics.

3 Challenges and future directions

As previously mentioned, the OCT image modality provides a great diagnosing aid for many organs. It is used in a wide range for diagnosing retinal diseases, such as glaucoma, CSC, AION, DME, and CME. Many studies were conducted to extract some specific features from OCT retinal images to diagnosis some diseases. In this section, we will discuss some challenges, which are currently facing the analysis of OCT retinal images. In addition, some future research directions will be discussed briefly in the sequent points.

3.1 Automatic segmentation techniques

OCT devices nowadays produce a large number of images. This large number of images make it difficult for humans to investigate. In addition, the existence of speckle noise, low image contrast, irregular shapes, morphological features (retinal detachment, MHs, drusen), and accurate manual segmentation of retinal layers is considered as a difficult task [57]. So, there is a need to produce automatic segmentation techniques to handle this large number of images. Automatic segmentation techniques can reduce time and effort. Also, they can provide repeatable and quantitative results [74]. They should be accurate and robust to image degeneration and low signal to noise ratio. It can allow early diagnosis or therapy monitoring. Thickness measurements are necessary for detecting pathological changes and diagnosing of retinal diseases [40]. Nevertheless, a few segmentation approaches have been developed, which addressed the problem of layers that are either invisible or missing [56, 75]. The proposed technique should be robust with respect to different types of OCT scanners from different manufacturers. They also should be robust with respect to the presence of blood vessel artifacts in the OCT images [5].

3.2 OCT CAD systems

Regarding the current work in OCT CAD systems, the experimental results show that these systems are used in off-line clinical or pathology studies. Therefore, additional speedup is required for OCT CAD systems to become suitable for clinical practice [35].

3.3 Standard number of layers

As far as we know, there is no standard number of detected layers in OCT retinal images. Some studies prefer to define all intraretinal layer, whereas other studies prefer only to define the most critical retina layers that are needed to identify a disease.

3.4 Weak layer boundaries

The target layers in the retina lack strong boundaries, which are surrounded by tissues with similar intensity profile. In addition, many objects are laying in a small region [41, 76].

3.5 Artifacts

There are many types of artifacts that are found in OCT images. Intensity inhomogeneity is considered as an important reason that significantly affects the accuracy of the segmentation process of the retina layers [77]. There are many reasons for intensity inhomogeneity in OCT images, such as poor scan quality, after multiframe averaging, opacity of transparent ocular media, off-center acquisitions, and vignetting due to misalignment. This problem negatively affects the performance of the used processing techniques, especially the segmentation process. Finally, little work had been done to correct this issue [6].

4 Conclusion

OCT is one of the fastest developing image modalities, especially in the last decade. OCT images have made it easier to differentiate between the anatomy of diseased and normal retina. This difference can be used to detect the early signs of many retinal diseases making OCT a very valuable modality. It can also be used to monitor the effect of the treatment on different parts of the retina. As we can see from this chapter, every disease has some spatial features that can be detected easily using OCT. In this chapter, we discussed how OCT could detect and define the structure of diseased and healthy eyes. Also, we reviewed some of the recent publications that demonstrate the ability of OCT in detecting and diagnosing a lot of retinal diseases. Also, we pointed out some of the challenges that face researchers in extracting and analyzing the information extracted from the OCT images. The promising experimental results are promising as shown in our review, which suggests that OCT is a reliable modality that can help in detecting and diagnosing retinal diseases even in its early stage.

This work could also be applied to various other applications in medical imaging, such as kidney, heart, prostate, lung, and brain in addition to the retina, as well as several non-medical applications [78–81].

One application is renal transplant functional assessment, especially with developing noninvasive CAD systems for renal transplant function assessment, utilizing different image modalities (e.g., ultrasound, computed tomography, MRI, etc.). Accurate assessment of renal transplant function is critically important for graft survival. Although transplantation can improve a patient well-being, there is a potential posttransplantation risk of kidney dysfunction that, if not treated in a timely manner, can lead to the loss of the entire graft, and even patient death. In particular, dynamic and diffusion MRI-based systems have been clinically used to assess transplanted kidneys with the advantage of providing information on each kidney separately. For more details about renal transplant functional assessment, the readers are referred to Refs. [82–109].

The heart is also an important application to this work. The clinical assessment of myocardial perfusion plays a major role in the diagnosis, management, and prognosis of ischemic heart disease patients. Thus, there have been ongoing efforts to develop automated systems for accurate analysis of myocardial perfusion using first-pass images [110–126].

Abnormalities of the lung could also be another promising area of research and a related application to this work. Radiation-induced lung injury is the main side effect of radiation therapy for lung cancer patients. Although higher radiation doses increase the radiation therapy effectiveness for tumor control, this can lead to lung injury as a greater quantity of normal lung tissues is included in the treated area. Almost one-third of patients who undergo radiation therapy develop lung injury following radiation treatment. The severity of radiation-induced lung injury ranges from ground-glass opacities and consolidation at the early phase to fibrosis and traction bronchiectasis in the late phase. Early detection of lung injury will thus help to improve management of the treatment [127–169].

This work can also be applied to other brain abnormalities, such as dyslexia in addition to autism. Dyslexia is one of the most complicated developmental brain disorders that affect children's learning abilities. Dyslexia leads to the failure to develop age-appropriate reading skills in spite of the normal intelligence level and adequate reading instructions. Neuropathological studies have revealed an abnormal anatomy of some structures, such as the corpus callosum in dyslexic brains. There has been a lot of work in the literature that aims at developing CAD systems for diagnosing such disorder, along with other brain disorders [170–192].

For the vascular system [193], this work could also be applied for the extraction of blood vessels, for example, from phase contrast magnetic resonance angiography (MRA). Accurate cerebrovascular segmentation using noninvasive MRA is crucial for the early diagnosis and timely treatment of intracranial vascular diseases [175, 176, 194–199].

References

- [1] D. Huang, E.A. Swanson, C.P. Lin, J.S. Schuman, W.G. Stinson, W. Chang, M.R. Hee, T. Flotte, K. Gregory, C.A. Puliafito, et al., Optical coherence tomography, *Science* 254 (5035) (1991) 1178–1181, <https://doi.org/10.1126/science.1957169>.
- [2] R.A. Gabbay, S. Sivarajah, Optical coherence tomography-based continuous noninvasive glucose monitoring in patients with diabetes, *Diabetes Technol. Ther.* 10 (3) (2008) 188–193, <https://doi.org/10.1089/dia.2007.0277>.
- [3] R.V. Kuranov, J. Qiu, A.B. McElroy, A. Estrada, A. Salvaggio, J. Kiel, A.K. Dunn, T.Q. Duong, T.E. Milner, Depth-resolved blood oxygen saturation measurement by dual-wavelength photothermal (DWP) optical coherence tomography, *Biomed. Opt. Express* 2 (3) (2011) 491–504, <https://doi.org/10.1364/BOE.2.000491>.
- [4] V. Kajić, B. Považay, B. Hermann, B. Hofer, D. Marshall, P.L. Rosin, W. Drexler, Robust segmentation of intraretinal layers in the normal human fovea using a novel statistical model based on texture and shape analysis, *Opt. Express* 18 (14) (2010) 14730–14744, <https://doi.org/10.1364/OE.18.014730>.
- [5] R. Kafieh, H. Rabbani, M.D. Abramoff, M. Sonka, Intra-retinal layer segmentation of 3D optical coherence tomography using coarse grained diffusion map, *Med. Image Anal.* 17 (8) (2013) 907–928, <https://doi.org/10.1016/j.media.2013.05.006>.
- [6] A. Lang, A. Carass, M. Hauser, E.S. Sotirchos, P.A. Calabresi, H.S. Ying, J.L. Prince, Retinal layer segmentation of macular OCT images using boundary classification. *Biomed. Opt. Express* 4 (7) (2013) 1133–1152, <https://doi.org/10.1364/BOE.4.001133>.

- [7] J. Cheng, D. Tao, Y. Quan, D.W.K. Wong, G.C.M. Cheung, M. Akiba, J. Liu, Speckle reduction in 3D optical coherence tomography of retina by A-scan reconstruction, *IEEE Trans. Med. Imaging* 35 (2016) 2270–2279, <https://doi.org/10.1109/TMI.2016.2556080>.
- [8] M.W. Jenkins, M. Watanabe, A.M. Rollins, Longitudinal imaging of heart development with optical coherence tomography, *IEEE J. Sel. Top. Quantum Electron.* 18 (3) (2012) 1166–1175.
- [9] B. Potsaid, I. Gorczynska, V.J. Srinivasan, Y. Chen, J. Jiang, A. Cable, J.G. Fujimoto, Ultrahigh speed spectral/Fourier domain OCT ophthalmic imaging at 70,000 to 312,500 axial scans per second, *Opt. Express* 16 (19) (2008) 15149–15169.
- [10] M.E.J. van Velthoven, D.J. Faber, F.D. Verbraak, T.G. van Leeuwen, M.D. de Smet, Recent developments in optical coherence tomography for imaging the retina, *Prog. Retin. Eye Res.* 26 (1) (2007) 57–77.
- [11] S.A. Boppart, G.J. Tearney, B.E. Bouma, J.F. Southern, M.E. Brezinski, J.G. Fujimoto, Noninvasive assessment of the developing *Xenopus* cardiovascular system using optical coherence tomography, *Proc. Natl Acad. Sci. USA* 94 (9) (1997) 4256–4261.
- [12] M.J. Suter, S.K. Nadkarni, G. Weisz, A. Tanaka, F.A. Jaffer, B.E. Bouma, G.J. Tearney, Intravascular optical imaging technology for investigating the coronary artery, *JACC Cardiovasc. Imaging* 4 (9) (2011) 1022–1039.
- [13] G.J. Tearney, M.E. Brezinski, J.G. Fujimoto, N.J. Weissman, S.A. Boppart, B.E. Bouma, J.F. Southern, Scanning single-mode fiber optic catheter-endoscope for optical coherence tomography, *Opt. Lett.* 21 (7) (1996) 543–545.
- [14] G.J. Tearney, M.E. Brezinski, B.E. Bouma, S.A. Boppart, C. Pitris, J.F. Southern, J.G. Fujimoto, In vivo endoscopic optical biopsy with optical coherence tomography, *Science* 276 (5321) (1997) 2037–2039.
- [15] T. Gambichler, G. Moussa, M. Sand, D. Sand, P. Altmeyer, K. Hoffmann, Applications of optical coherence tomography in dermatology, *J. Dermatol. Sci.* 40 (2) (2005) 85–94.
- [16] J.M. Schmitt, M.J. Yadlowsky, R.F. Bonner, Subsurface imaging of living skin with optical coherence microscopy, *Dermatology* 191 (2) (1995) 93–98.
- [17] K.D. Rao, Y. Verma, H.S. Patel, P.K. Gupta, Non-invasive ophthalmic imaging of adult zebrafish eye using optical coherence tomography, *Curr. Sci.* 90 (11) (2006) 1506.
- [18] L. Kagemann, H. Ishikawa, J. Zou, P. Charukamnoetkanok, G. Wollstein, K.A. Townsend, M. L. Gabriele, N. Bahary, X. Wei, J.G. Fujimoto, et al., Repeated, noninvasive, high resolution spectral domain optical coherence tomography imaging of zebrafish embryos, *Mol. Vis.* 14 (2008) 2157–2170.
- [19] S.H. Syed, K.V. Larin, M.E. Dickinson, I.V. Larina, Optical coherence tomography for high-resolution imaging of mouse development in utero, *J. Biomed. Opt.* 16 (4) (2011) 046004.
- [20] J.C. Burton, S. Wang, C.A. Stewart, R.R. Behringer, I.V. Larina, High-resolution three-dimensional in vivo imaging of mouse oviduct using optical coherence tomography, *Biomed. Opt. Express* 6 (7) (2015) 2713–2723.
- [21] A. Alex, A. Li, X. Zeng, R.E. Tate, M.L. McKee, D.E. Capen, Z. Zhang, R.E. Tanzi, C. Zhou, A circadian clock gene, *Cry*, affects heart morphogenesis and function in *Drosophila* as revealed by optical coherence microscopy, *PLoS ONE* 10 (9) (2015) e0137236.
- [22] A.P. Yow, J. Cheng, A. Li, C. Wall, D.W.K. Wong, J. Liu, H.L. Tey, Skin surface topographic assessment using in vivo high-definition optical coherence tomography, in: 2015 10th International Conference on Information, Communications and Signal Processing (ICICS), December, 2015, pp. 1–4, <https://doi.org/10.1109/ICICS.2015.7459853>.
- [23] A. Li, J. Cheng, A.P. Yow, C. Wall, D.W.K. Wong, H.L. Tey, J. Liu, Epidermal segmentation in high-definition optical coherence tomography, in: 2015 37th Annual International Conference of the IEEE Engineering in Medicine and Biology Society (EMBC), August, 2015, pp. 3045–3048, ISSN 1094-687X, <https://doi.org/10.1109/EMBC.2015.7319034>.

- [24] S.S. Akhouri, L.N. Darlow, Extracting subsurface fingerprints using optical coherence tomography, in: 2015 Third International Conference on Digital Information, Networking, and Wireless Communications (DINWC), February, 2015, pp. 184–187, <https://doi.org/10.1109/DINWC.2015.7054240>.
- [25] M. Xu, J. Cheng, D.W.K. Wong, J. Liu, A. Taruya, A. Tanaka, Graph based lumen segmentation in optical coherence tomography images, in: 2015 10th International Conference on Information, Communications and Signal Processing (ICICS), December, 2015, pp. 1–5, <https://doi.org/10.1109/ICICS.2015.7459951>.
- [26] R. Shalev, D. Prabhu, K. Tanaka, A.M. Rollins, M. Costa, H.G. Bezerra, R. Soumya, D.L. Wilson, Intravascular optical coherence tomography image analysis method, in: 2015 41st Annual Northeast Biomedical Engineering Conference (NEBEC), April, 2015, pp. 1–2, ISSN 2160-6986, <https://doi.org/10.1109/NEBEC.2015.7117058>.
- [27] C. Kut, K.L. Chaichana, J. Xi, S.M. Raza, X. Ye, E.R. McVeigh, F.J. Rodriguez, A. Quiñones-Hinojosa, X. Li, Detection of human brain cancer infiltration ex vivo and in vivo using quantitative optical coherence tomography, *Sci. Transl. Med.* 7 (292) (2015) 292ra100.
- [28] V.J. Srinivasan, E.T. Mandeville, A. Can, F. Blasi, M. Climov, A. Daneshmand, J.H. Lee, E. Yu, H. Radhakrishnan, E.H. Lo, et al., Multiparametric, longitudinal optical coherence tomography imaging reveals acute injury and chronic recovery in experimental ischemic stroke, *PLoS ONE* 8 (8) (2013) e71478.
- [29] R.A. Leitgeb, M. Villiger, A.H. Bachmann, L. Steinmann, T. Lasser, Extended focus depth for Fourier domain optical coherence microscopy, *Opt. Lett.* 31 (16) (2006) 2450–2452.
- [30] F. Li, Y. Song, A. Dryer, W. Cogguillo, Y. Berdichevsky, C. Zhou, Nondestructive evaluation of progressive neuronal changes in organotypic rat hippocampal slice cultures using ultrahigh-resolution optical coherence microscopy, *Neurophotonics* 1 (2) (2014) 025002.
- [31] C. Leahy, H. Radhakrishnan, V.J. Srinivasan, Volumetric imaging and quantification of cytoarchitecture and myeloarchitecture with intrinsic scattering contrast, *Biomed. Opt. Express* 4 (10) (2013) 1978–1990.
- [32] V.J. Srinivasan, H. Radhakrishnan, J.Y. Jiang, S. Barry, A.E. Cable, Optical coherence microscopy for deep tissue imaging of the cerebral cortex with intrinsic contrast, *Opt. Express* 20 (3) (2012) 2220–2239.
- [33] O. Assayag, K. Grieve, B. Devaux, F. Harms, J. Pallud, F. Chretien, C. Boccara, P. Varlet, Imaging of non-tumorous and tumorous human brain tissues with full-field optical coherence tomography, *NeuroImage Clin.* 2 (2013) 549–557.
- [34] C. Magnain, J.C. Augustinack, E. Konukoglu, M.P. Frosch, S. Sakadžić, A. Varjabedian, N. Garcia, V.J. Wedeen, D.A. Boas, B. Fischl, Optical coherence tomography visualizes neurons in human entorhinal cortex, *Neurophotonics* 2 (1) (2015) 015004.
- [35] F. Shi, X. Chen, H. Zhao, W. Zhu, D. Xiang, E. Gao, M. Sonka, H. Chen, Automated 3-D retinal layer segmentation of macular optical coherence tomography images with serous pigment epithelial detachments, *IEEE Trans. Med. Imaging* 34 (2) (2015) 441–452, <https://doi.org/10.1109/TMI.2014.2359980>.
- [36] J. Sugmk, S. Kiattisin, A. Leelasanthitham, Automated classification between age-related macular degeneration and diabetic macular edema in OCT image using image segmentation, in: 2014 Seventh Biomedical Engineering International Conference (BMEiCON), November, 2014, pp. 1–4, <https://doi.org/10.1109/BMEiCON.2014.7017441>.
- [37] J. Novosel, Z. Wang, H. de Jong, M. van Velthoven, K.A. Vermeer, L.J. van Vliet, Locally-adaptive loosely-coupled level sets for retinal layer and fluid segmentation in subjects with central serous retinopathy, in: 2016 IEEE 13th International Symposium on Biomedical Imaging (ISBI), April, 2016, pp. 702–705, <https://doi.org/10.1109/ISBI.2016.7493363>.

- [38] H. Ishikawa, D.M. Stein, G. Wollstein, S. Beaton, J.G. Fujimoto, J.S. Schuman, Macular segmentation with optical coherence tomography, *Invest. Ophthalmol. Vis. Sci.* 46 (6) (2005) 2012–2017.
- [39] M.K. Garvin, M.D. Abramoff, X. Wu, S.R. Russell, T.L. Burns, M. Sonka, Automated 3-D intraretinal layer segmentation of macular spectral-domain optical coherence tomography images, *IEEE Trans. Med. Imaging* 28 (9) (2009) 1436–1447, <https://doi.org/10.1109/TMI.2009.2016958>.
- [40] A.M. Bagci, M. Shahidi, R. Ansari, M. Blair, N.P. Blair, R. Zelkha, Thickness profiles of retinal layers by optical coherence tomography image segmentation, *Am. J. Ophthalmol.* 146 (5) (2008) 679–687. e1, <https://doi.org/10.1016/j.ajo.2008.06.010>.
- [41] S. Lu, C.Y.L. Cheung, J. Liu, J.H. Lim, C.K.S. Leung, T.Y. Wong, Automated layer segmentation of optical coherence tomography images, *IEEE Trans. Biomed. Eng.* 57 (10) (2010) 2605–2608, <https://doi.org/10.1109/TBME.2010.2055057>.
- [42] F. Rossant, I. Ghorbel, I. Bloch, M. Paques, S. Tick, Automated segmentation of retinal layers in OCT imaging and derived ophthalmic measures, in: 2009 IEEE International Symposium on Biomedical Imaging: From Nano to Macro, June, 2009, pp. 1370–1373, ISSN 1945-7928, <https://doi.org/10.1109/ISBI.2009.5193320>.
- [43] Q. Yang, C.A. Reisman, Z. Wang, Y. Fukuma, M. Hangai, N. Yoshimura, A. Tomidokoro, M. Araie, A.S. Raza, D.C. Hood, K. Chan, Automated layer segmentation of macular OCT images using dual-scale gradient information, *Opt. Express* 18 (20) (2010) 21293–21307.
- [44] A. ElTanboly, M. Ismail, A. Shalaby, A. Switala, A. El-Baz, S. Schaal, G. Gimelfarb, M. El-Azab, A computer-aided diagnostic system for detecting diabetic retinopathy in optical coherence tomography images, *Med. Phys.* 44 (3) (2017) 914–923.
- [45] R. Brancato, B. Lumbroso, Guide to Optical Coherence Tomography Interpretation, I.N.C Innovation-News Communication, 2004, ISBN 9788886193412, Available from: <https://books.google.com/books?id=x-ZiQgAACAAJ>.
- [46] J.S. Schuman, C.A. Puliafito, J.G. Fujimoto, Optical Coherence Tomography of Ocular Diseases, SLACK Incorporated, 2004, ISBN 9781556426094, Available from: <https://books.google.com/books?id=SjhpQgAACAAJ>.
- [47] D. Koleva-Georgieva, Optical Coherence Tomography Findings in Diabetic Macular Edema, INTECH Open Access Publisher, Rijeka, 2012.
- [48] M. Salarian, R. Ansari, J. Wanek, M. Shahidi, Accurate segmentation of retina nerve fiber layer in OCT images, in: 2015 IEEE International Conference on Electro/Information Technology (EIT), May, 2015, pp. 653–656, ISSN 2154-0357, <https://doi.org/10.1109/EIT.2015.7293411>.
- [49] S. Roychowdhury, D.D. Koozekanani, M. Reinsbach, K.K. Parhi, 3-D localization of diabetic macular edema using OCT thickness maps, in: 2015 37th Annual International Conference of the IEEE Engineering in Medicine and Biology Society (EMBC), August, 2015, pp. 4334–4337, ISSN 1094-687X, <https://doi.org/10.1109/EMBC.2015.7319354>.
- [50] S. Lee, E. Lebed, M.V. Sarunic, M.F. Beg, Exact surface registration of retinal surfaces from 3-D optical coherence tomography images, *IEEE Trans. Biomed. Eng.* 62 (2) (2015) 609–617, <https://doi.org/10.1109/TBME.2014.2361778>.
- [51] K.A. Vermeer, J. van der Schoot, H.G. Lemij, J.F. de Boer, Automated segmentation by pixel classification of retinal layers in ophthalmic OCT images, *Biomed. Opt. Express* 2 (6) (2011) 1743–1756.
- [52] H. Bogunović, M. Sonka, Y.H. Kwon, P. Kemp, M.D. Abramoff, X. Wu, Multi-surface and multi-field co-segmentation of 3-D retinal optical coherence tomography, *IEEE Trans. Med. Imaging* 33 (12) (2014) 2242–2253.
- [53] S.-E. Ahn, J. Oh, J.-H. Oh, I.K. Oh, S.-W. Kim, K. Huh, Three-dimensional configuration of subretinal fluid in central serous chorioretinopathy 3-dimensional configuration of subretinal fluid, *Invest. Ophthalmol. Vis. Sci.* 54 (9) (2013) 5944–5952.

- [54] C.M. Eandi, J.E. Chung, F. Cardillo-Piccolino, R.F. Spaide, Optical coherence tomography in unilateral resolved central serous chorioretinopathy, *Retina* 25 (4) (2005), ISSN 0275-004X.
- [55] Y. Imamura, T. Fujiwara, R. Margolis, R. Spaide, Enhanced depth imaging optical coherence tomography of the choroid in central serous chorioretinopathy, *Retina* 29 (10) (2009), ISSN 0275-004X.
- [56] J. Novosel, K.A. Vermeer, L. Pierrache, C.C.W. Klaver, L.I. van den Born, L.J. van Vliet, Method for segmentation of the layers in the outer retina, in: 2015 37th Annual International Conference of the IEEE Engineering in Medicine and Biology Society (EMBC), August, 2015, pp. 5646–5649, ISSN 1094-687X, <https://doi.org/10.1109/EMBC.2015.7319673>.
- [57] M.K. Garvin, M.D. Abramoff, R. Kardon, S.R. Russell, X. Wu, M. Sonka, Intraretinal layer segmentation of macular optical coherence tomography images using optimal 3-D graph search, *IEEE Trans. Med. Imaging* 27 (10) (2008) 1495–1505, <https://doi.org/10.1109/TMI.2008.923966>.
- [58] T.R. Hedges, L.N. Vuong, A.O. Gonzalez-Garcia, C.E. Mendoza-Santiesteban, M.L. Amaro-Quierza, Subretinal fluid from anterior ischemic optic neuropathy demonstrated by optical coherence tomography, *Arch. Ophthalmol.* 126 (6) (2008) 812–815.
- [59] R. Varma, N.M. Bressler, Q.V. Doan, et al., Prevalence of and risk factors for diabetic macular edema in the United States, *JAMA Ophthalmol.* 132 (11) (2014) 1334–1340, <https://doi.org/10.1001/jamaophthalmol.2014.2854>.
- [60] A. Correia, L. Pinto, A. Araújo, S. Barbeiro, F. Caramelo, P. Menezes, M. Morgado, P. Serranho, R. Bernardes, Monte Carlo simulation of diabetic macular edema changes on optical coherence tomography data, in: IEEE-EMBS International Conference on Biomedical and Health Informatics (BHI), IEEE, 2014, pp. 724–727.
- [61] G.R. Wilkins, O.M. Houghton, A.L. Oldenburg, Automated segmentation of intraretinal cystoid fluid in optical coherence tomography, *IEEE Trans. Biomed. Eng.* 59 (4) (2012) 1109–1114, <https://doi.org/10.1109/TBME.2012.2184759>.
- [62] S. Roychowdhury, D.D. Koozekanani, S. Radwan, K.K. Parhi, Automated localization of cysts in diabetic macular edema using optical coherence tomography images, in: 2013 35th Annual International Conference of the IEEE Engineering in Medicine and Biology Society (EMBC), IEEE, 2013, pp. 1426–1429.
- [63] A.M. Abhishek, T.T.J.M. Berendschot, S.V. Rao, S. Dabir, Segmentation and analysis of retinal layers (ILM & RPE) in optical coherence tomography images with edema, in: 2014 IEEE Conference on Biomedical Engineering and Sciences (IECBES), December, 2014, pp. 204–209, <https://doi.org/10.1109/IECBES.2014.7047486>.
- [64] T.G. Rotsos, M.M. Moschos, Cystoid macular edema, *Clin. Ophthalmol.* 2 (2008) 919–930.
- [65] H. Faghihi, F. Ghassemi, K.G. Falavarjani, G.S. Anari, M. Safizadeh, K. Shahraki, Spontaneous closure of traumatic macular holes, *Can. J. Ophthalmol.* 49 (4) (2014) 395–398.
- [66] L. Zhang, K. Lee, M. Niemeijer, R.F. Mullins, M. Sonka, M.D. Abramoff, Automated segmentation of the choroid from clinical SD-OCT automated segmentation of choroid from SD-OCT, *Invest. Ophthalmol. Vis. Sci.* 53 (12) (2012) 7510, <https://doi.org/10.1167/iovs.12-10311>.
- [67] N. Slokom, H. Trabelsi, I. Zghal, Segmentation of cystoid macular edema in optical coherence tomography, in: 2016 2nd International Conference on Advanced Technologies for Signal and Image Processing (ATSIP), March, 2016, pp. 303–306, <https://doi.org/10.1109/ATSIP.2016.7523096>.
- [68] Q. Chen, T. Leng, L. Zheng, L. Kutzscher, J. Ma, L. de Sisternes, D.L. Rubin, Automated drusen segmentation and quantification in SD-OCT images, *Med. Image Anal.* 17 (8) (2013) 1058–1072, <https://doi.org/10.1016/j.media.2013.06.003>.
- [69] P.A. Keane, P.J. Patel, S. Liakopoulos, F.M. Heussen, S.R. Sadda, A. Tufail, Evaluation of age-related macular degeneration with optical coherence tomography, *Surv. Ophthalmol.* 57 (5) (2012) 389–414, <https://doi.org/10.1016/j.survophthal.2012.01.006>.

- [70] A.A. Khanifar, A.F. Koreishi, J.A. Izatt, C.A. Toth, Drusen ultrastructure imaging with spectral domain optical coherence tomography in age-related macular degeneration, *Ophthalmology* 115 (11) (2008) 1883–1890. e1, <https://doi.org/10.1016/j.ophtha.2008.04.041>.
- [71] S.G. Schuman, A.F. Koreishi, S. Farsiu, S. Ho Jung, J.A. Izatt, C.A. Toth, Photoreceptor layer thinning over drusen in eyes with age-related macular degeneration imaged in vivo with spectral-domain optical coherence tomography, *Ophthalmology* 116 (3) (2009) 488–496. e2, <https://doi.org/10.1016/j.ophtha.2008.10.006>.
- [72] J. Oliveira, S. Pereira, L. Gonçalves, M. Ferreira, C.A. Silva, Sparse high order potentials for extending multi-surface segmentation of OCT images with drusen, in: 2015 37th Annual International Conference of the IEEE Engineering in Medicine and Biology Society (EMBC), August, 2015, pp. 2952–2955, ISSN 1094-687X, <https://doi.org/10.1109/EMBC.2015.7319011>.
- [73] A. ElTanboly, A. Placio, A. Shalaby, A. Switala, O. Helmy, S. Schaal, A. El-Baz, An automated approach for early detection of diabetic retinopathy using SD-OCT images, *Front. Biosci. (Elite Ed.)* 10 (2018) 197–207.
- [74] A. Yazdanpanah, G. Hamarneh, B.R. Smith, M.V. Sarunic, Segmentation of intra-retinal layers from optical coherence tomography images using an active contour approach, *IEEE Trans. Med. Imaging* 30 (2) (2011) 484–496, <https://doi.org/10.1109/TMI.2010.2087390>.
- [75] L. Ngo, G. Yih, S. Ji, J.H. Han, A study on automated segmentation of retinal layers in optical coherence tomography images, in: 2016 4th International Winter Conference on Brain-Computer Interface (BCI), February, 2016, pp. 1–2, <https://doi.org/10.1109/IWW-BCI.2016.7457465>.
- [76] Q. Song, J. Bai, M.K. Garvin, M. Sonka, J.M. Buatti, X. Wu, Optimal multiple surface segmentation with shape and context priors, *IEEE Trans. Med. Imaging* 32 (2) (2013) 376–386.
- [77] I.C. Han, G.J. Jaffe, Evaluation of artifacts associated with macular spectral-domain optical coherence tomography, *Ophthalmology* 117 (6) (2010) 1177–1189. e4, <https://doi.org/10.1016/j.ophtha.2009.10.029>.
- [78] A.H. Mahmoud, Utilizing Radiation for Smart Robotic Applications Using Visible, Thermal, and Polarization Images (Ph.D. dissertation), University of Louisville, 2014.
- [79] A. Mahmoud, A. El-Barkouky, J. Graham, A. Farag, Pedestrian detection using mixed partial derivative based histogram of oriented gradients, in: 2014 IEEE International Conference on Image Processing (ICIP), IEEE, 2014, pp. 2334–2337.
- [80] A. El-Barkouky, A. Mahmoud, J. Graham, A. Farag, An interactive educational drawing system using a humanoid robot and light polarization, in: 2013 IEEE International Conference on Image Processing, IEEE, 2013, pp. 3407–3411.
- [81] A.H. Mahmoud, M.T. El-Melegy, A.A. Farag, Direct method for shape recovery from polarization and shading, in: 2012 19th IEEE International Conference on Image Processing, IEEE, 2012, pp. 1769–1772.
- [82] A.M. Ali, A.A. Farag, A. El-Baz, Graph cuts framework for kidney segmentation with prior shape constraints, in: Proceedings of International Conference on Medical Image Computing and Computer-Assisted Intervention (MICCAI'07), Brisbane, Australia, October 29–November 2, vol. 1, 2007, pp. 384–392.
- [83] A.S. Chowdhury, R. Roy, S. Bose, F.K.A. Elnakib, A. El-Baz, Non-rigid biomedical image registration using graph cuts with a novel data term, in: Proceedings of IEEE International Symposium on Biomedical Imaging: From Nano to Macro (ISBI'12), Barcelona, Spain, May 2–5, 2012, pp. 446–449.
- [84] A. El-Baz, A.A. Farag, S.E. Yuksel, M.E.A. El-Ghar, T.A. Eldiasty, M.A. Ghoneim, Application of deformable models for the detection of acute renal rejection, in: *Deformable Models*, Springer, New York, NY, 2007, pp. 293–333.
- [85] A. El-Baz, A. Farag, R. Fahmi, S. Yuksel, M.A. El-Ghar, T. Eldiasty, Image analysis of renal DCE MRI for the detection of acute renal rejection, in: Proceedings of IAPR International Conference on Pattern Recognition (ICPR'06), Hong Kong, August 20–24, 2006, pp. 822–825.

- [86] A. El-Baz, A. Farag, R. Fahmi, S. Yuksel, W. Miller, M.A. El-Ghar, T. El-Diasty, M. Ghoneim, A new CAD system for the evaluation of kidney diseases using DCE-MRI, in: *Proceedings of International Conference on Medical Image Computing and Computer-Assisted Intervention (MICCAI'08)*, Copenhagen, Denmark, October 1–6, 2006, pp. 446–453.
- [87] A. El-Baz, G. Gimel'farb, M.A. El-Ghar, A novel image analysis approach for accurate identification of acute renal rejection, in: *Proceedings of IEEE International Conference on Image Processing (ICIP'08)*, San Diego, California, USA, October 12–15, 2008, pp. 1812–1815.
- [88] A. El-Baz, G. Gimel'farb, M.A. El-Ghar, Image analysis approach for identification of renal transplant rejection, in: *Proceedings of IAPR International Conference on Pattern Recognition (ICPR'08)*, Tampa, Florida, USA, December 8–11, 2008, pp. 1–4.
- [89] A. El-Baz, G. Gimel'farb, M.A. El-Ghar, New Motion correction models for automatic identification of renal transplant rejection, in: *Proceedings of International Conference on Medical Image Computing and Computer-Assisted Intervention (MICCAI'07)*, Brisbane, Australia, October 29–November 2, 2007, pp. 235–243.
- [90] A. Farag, A. El-Baz, S. Yuksel, M.A. El-Ghar, T. Eldiasty, A framework for the detection of acute rejection with dynamic contrast enhanced magnetic resonance imaging, in: *Proceedings of IEEE International Symposium on Biomedical Imaging: From Nano to Macro (ISBI'06)*, Arlington, Virginia, USA, April 6–9, 2006, pp. 418–421.
- [91] F. Khalifa, G.M. Beache, M.A. El-Ghar, T. El-Diasty, G. Gimel'farb, M. Kong, A. El-Baz, Dynamic contrast-enhanced MRI-based early detection of acute renal transplant rejection, *IEEE Trans. Med. Imaging* 32 (10) (2013) 1910–1927.
- [92] F. Khalifa, A. El-Baz, G. Gimel'farb, M.A. El-Ghar, Non-invasive image-based approach for early detection of acute renal rejection, in: *Proceedings of International Conference Medical Image Computing and Computer-Assisted Intervention (MICCAI'10)*, Beijing, China, September 20–24, 2010, pp. 10–18.
- [93] F. Khalifa, A. El-Baz, G. Gimel'farb, R. Ouseph, M.A. El-Ghar, Shape-appearance guided level-set deformable model for image segmentation, in: *Proceedings of IAPR International Conference on Pattern Recognition (ICPR'10)*, Istanbul, Turkey, August 23–26, 2010, pp. 4581–4584.
- [94] F. Khalifa, M.A. El-Ghar, B. Abdollahi, H. Frieboes, T. El-Diasty, A. El-Baz, A comprehensive non-invasive framework for automated evaluation of acute renal transplant rejection using DCE-MRI, *NMR Biomed.* 26 (11) (2013) 1460–1470.
- [95] F. Khalifa, M.A. El-Ghar, B. Abdollahi, H.B. Frieboes, T. El-Diasty, A. El-Baz, Dynamic contrast-enhanced MRI-based early detection of acute renal transplant rejection, in: *2014 Annual Scientific Meeting and Educational Course Brochure of the Society of Abdominal Radiology (SAR'14)*, Boca Raton, Florida, March 23–28, 2014, p. CID:1855912.
- [96] F. Khalifa, A. Elnakib, G.M. Beache, G. Gimel'farb, M.A. El-Ghar, G. Sokhadze, S. Manning, P. McClure, A. El-Baz, 3D kidney segmentation from CT images using a level set approach guided by a novel stochastic speed function, in: *Proceedings of International Conference Medical Image Computing and Computer-Assisted Intervention (MICCAI'11)*, Toronto, Canada, September 18–22, 2011, pp. 587–594.
- [97] F. Khalifa, G. Gimel'farb, M.A. El-Ghar, G. Sokhadze, S. Manning, P. McClure, R. Ouseph, A. El-Baz, A new deformable model-based segmentation approach for accurate extraction of the kidney from abdominal CT images, in: *Proceedings of IEEE International Conference on Image Processing (ICIP'11)*, Brussels, Belgium, September 11–14, 2011, pp. 3393–3396.
- [98] M. Mostapha, F. Khalifa, A. Alansary, A. Soliman, J. Suri, A. El-Baz, Computer-aided diagnosis systems for acute renal transplant rejection: challenges and methodologies, in: A. El-Baz, L. Saba, J. Suri (Eds.), *Abdomen and Thoracic Imaging*, Springer, 2014, pp. 1–35.
- [99] M. Shehata, F. Khalifa, E. Hollis, A. Soliman, E. Hosseini-Asl, M.A. El-Ghar, M. El-Baz, A.C. Dwyer, A. El-Baz, R. Keynton, A new non-invasive approach for early classification of renal rejection types using diffusion-weighted MRI, in: *IEEE International Conference on Image Processing (ICIP)*, IEEE, 2016, pp. 136–140.

- [100] F. Khalifa, A. Soliman, A. Takieldeem, M. Shehata, M. Mostapha, A. Shaffie, R. Ouseph, A. Elmaghraby, A. El-Baz, Kidney segmentation from CT images using a 3D NMF-guided active contour model, in: IEEE 13th International Symposium on Biomedical Imaging (ISBI), IEEE, 2016, pp. 432–435.
- [101] M. Shehata, F. Khalifa, A. Soliman, A. Takieldeem, M.A. El-Ghar, A. Shaffie, A.C. Dwyer, R. Ouseph, A. El-Baz, R. Keynton, 3D diffusion MRI-based CAD system for early diagnosis of acute renal rejection, in: 2016 IEEE 13th International Symposium on Biomedical Imaging (ISBI), IEEE, 2016, pp. 1177–1180.
- [102] M. Shehata, F. Khalifa, A. Soliman, R. Alrefai, M.A. El-Ghar, A.C. Dwyer, R. Ouseph, A. El-Baz, A level set-based framework for 3D kidney segmentation from diffusion MR images, in: IEEE International Conference on Image Processing (ICIP), IEEE, 2015, pp. 4441–4445.
- [103] M. Shehata, F. Khalifa, A. Soliman, M.A. El-Ghar, A.C. Dwyer, G. Gimel'farb, R. Keynton, A. El-Baz, A promising non-invasive CAD system for kidney function assessment, in: International Conference on Medical Image Computing and Computer-Assisted Intervention, Springer, 2016, pp. 613–621.
- [104] F. Khalifa, A. Soliman, A. Elmaghraby, G. Gimel'farb, A. El-Baz, 3D kidney segmentation from abdominal images using spatial-appearance models, *Comput. Math. Methods Med.* 2017 (2017) 1–10.
- [105] E. Hollis, M. Shehata, F. Khalifa, M.A. El-Ghar, T. El-Diasty, A. El-Baz, Towards non-invasive diagnostic techniques for early detection of acute renal transplant rejection: a review, *Egypt. J. Radiol. Nucl. Med.* 48 (1) (2016) 257–269.
- [106] M. Shehata, F. Khalifa, A. Soliman, M.A. El-Ghar, A.C. Dwyer, A. El-Baz, Assessment of renal transplant using image and clinical-based biomarkers, in: Proceedings of 13th Annual Scientific Meeting of American Society for Diagnostics and Interventional Nephrology (ASDIN'17), New Orleans, Louisiana, USA, February 10–12, 2017.
- [107] M. Shehata, F. Khalifa, A. Soliman, M.A. El-Ghar, A.C. Dwyer, A. El-Baz, Early assessment of acute renal rejection, in: Proceedings of 12th Annual Scientific Meeting of American Society for Diagnostics and Interventional Nephrology (ASDIN'16), Pheonix, Arizona, USA, February 19–21, 2016, 2017.
- [108] A. Eltanboly, M. Ghazal, H. Hajjdiab, A. Shalaby, A. Switala, A. Mahmoud, P. Sahoo, M. El-Azab, A. El-Baz, Level sets-based image segmentation approach using statistical shape priors, *Appl. Math. Comput.* 340 (2019) 164–179.
- [109] M. Shehata, A. Mahmoud, A. Soliman, F. Khalifa, M. Ghazal, M.A. El-Ghar, M. El-Melegy, A. El-Baz, 3D kidney segmentation from abdominal diffusion MRI using an appearance-guided deformable boundary, *PLoS ONE* 13 (7) (2018) e0200082.
- [110] F. Khalifa, G. Beache, A. El-Baz, G. Gimel'farb, Deformable model guided by stochastic speed with application in cine images segmentation, in: Proceedings of IEEE International Conference on Image Processing (ICIP'10), Hong Kong, September 26–29, 2010, pp. 1725–1728.
- [111] F. Khalifa, G.M. Beache, A. Elnakib, H. Sliman, G. Gimel'farb, K.C. Welch, A. El-Baz, A new shape-based framework for the left ventricle wall segmentation from cardiac first-pass perfusion MRI, in: Proceedings of IEEE International Symposium on Biomedical Imaging: From Nano to Macro (ISBI'13), San Francisco, California, USA, April 7–11, 2013, pp. 41–44.
- [112] F. Khalifa, G.M. Beache, A. Elnakib, H. Sliman, G. Gimel'farb, K.C. Welch, A. El-Baz, A new nonrigid registration framework for improved visualization of transmural perfusion gradients on cardiac first-pass perfusion MRI, in: Proceedings of IEEE International Symposium on Biomedical Imaging: From Nano to Macro (ISBI'12), Barcelona, Spain, May 2–5, 2012, pp. 828–831.
- [113] F. Khalifa, G.M. Beache, A. Firjani, K.C. Welch, G. Gimel'farb, A. El-Baz, A new nonrigid registration approach for motion correction of cardiac first-pass perfusion MRI, in: Proceedings of IEEE International Conference on Image Processing (ICIP'12), Lake Buena Vista, Florida, September 30–October 3, 2012, pp. 1665–1668.
- [114] F. Khalifa, G.M. Beache, G. Gimel'farb, A. El-Baz, A novel CAD system for analyzing cardiac first-pass MR images, in: Proceedings of IAPR International Conference on Pattern Recognition (ICPR'12), Tsukuba Science City, Japan, November 11–15, 2012, pp. 77–80.

- [115] F. Khalifa, G.M. Beache, G. Gimel'farb, A. El-Baz, A novel approach for accurate estimation of left ventricle global indexes from short-axis cine MRI, in: *Proceedings of IEEE International Conference on Image Processing (ICIP'11)*, Brussels, Belgium, September 11–14, 2011, pp. 2645–2649.
- [116] F. Khalifa, G.M. Beache, G. Gimel'farb, G.A. Giridharan, A. El-Baz, A new image-based framework for analyzing cine images, in: A. El-Baz, U.R. Acharya, M. Mirmedhdi, J.S. Suri (Eds.), *Handbook of Multi Modality State-of-the-Art Medical Image Segmentation and Registration Methodologies*, vol. 2, Springer, New York, NY, 2011, pp. 69–98, ISBN 978-1-4419-8203-2 (Chapter 3).
- [117] F. Khalifa, G.M. Beache, G. Gimel'farb, G.A. Giridharan, A. El-Baz, Accurate automatic analysis of cardiac cine images, *IEEE Trans. Biomed. Eng.* 59 (2) (2012) 445–455.
- [118] F. Khalifa, G.M. Beache, M. Nitzken, G. Gimel'farb, G.A. Giridharan, A. El-Baz, Automatic analysis of left ventricle wall thickness using short-axis cine CMR images, in: *Proceedings of IEEE International Symposium on Biomedical Imaging: From Nano to Macro (ISBI'11)*, Chicago, Illinois, March 30–April 2, 2011, pp. 1306–1309.
- [119] M. Nitzken, G. Beache, A. Elnakib, F. Khalifa, G. Gimel'farb, A. El-Baz, Accurate modeling of tagged CMR 3D image appearance characteristics to improve cardiac cycle strain estimation, in: *2012 19th IEEE International Conference on Image Processing (ICIP)*, Orlando, Florida, USA, September, IEEE, 2012, pp. 521–524.
- [120] M. Nitzken, G. Beache, A. Elnakib, F. Khalifa, G. Gimel'farb, A. El-Baz, Improving full-cardiac cycle strain estimation from tagged CMR by accurate modeling of 3D image appearance characteristics, in: *2012 9th IEEE International Symposium on Biomedical Imaging (ISBI)*, Barcelona, Spain, May, IEEE, 2012, pp. 462–465 (selected for oral presentation).
- [121] M.J. Nitzken, A.S. El-Baz, G.M. Beache, Markov-Gibbs random field model for improved full-cardiac cycle strain estimation from tagged CMR, *J. Cardiovasc. Magn. Reson.* 14 (1) (2012) 1–2.
- [122] H. Sliman, A. Elnakib, G.M. Beache, A. Elmaghraby, A. El-Baz, Assessment of myocardial function from cine cardiac MRI using a novel 4D tracking approach, *J. Comput. Sci. Syst. Biol.* 7 (2014) 169–173.
- [123] H. Sliman, A. Elnakib, G.M. Beache, A. Soliman, F. Khalifa, G. Gimel'farb, A. Elmaghraby, A. El-Baz, A novel 4D PDE-based approach for accurate assessment of myocardium function using cine cardiac magnetic resonance images, in: *Proceedings of IEEE International Conference on Image Processing (ICIP'14)*, Paris, France, October 27–30, 2014, pp. 3537–3541.
- [124] H. Sliman, F. Khalifa, A. Elnakib, G.M. Beache, A. Elmaghraby, A. El-Baz, A new segmentation-based tracking framework for extracting the left ventricle cavity from cine cardiac MRI, in: *Proceedings of IEEE International Conference on Image Processing (ICIP'13)*, Melbourne, Australia, September 15–18, 2013, pp. 685–689.
- [125] H. Sliman, F. Khalifa, A. Elnakib, A. Soliman, G.M. Beache, A. Elmaghraby, G. Gimel'farb, A. El-Baz, Myocardial borders segmentation from cine MR images using bi-directional coupled parametric deformable models, *Med. Phys.* 40 (9) (2013) 1–13.
- [126] H. Sliman, F. Khalifa, A. Elnakib, A. Soliman, G.M. Beache, G. Gimel'farb, A. Elmaghraby, A. El-Baz, Accurate segmentation framework for the left ventricle wall from cardiac cine MRI, in: *Proceedings of International Symposium on Computational Models for Life Science (CMLS'13)*, Sydney, Australia, November 27–29, vol. 1559, 2013, pp. 287–296.
- [127] B. Abdollahi, A.C. Civelek, X.-F. Li, J. Suri, A. El-Baz, PET/CT nodule segmentation and diagnosis: a survey, in: L. Saba, J.S. Suri (Eds.), *Multi Detector CT Imaging*, Taylor & Francis, 2014, pp. 639–651, ISBN 978-1-4398-9397-5 (Chapter 30).
- [128] B. Abdollahi, A. El-Baz, A.A. Amini, A multi-scale non-linear vessel enhancement technique, in: *2011 Annual International Conference of the IEEE Engineering in Medicine and Biology Society, EMBC*, IEEE, 2011, pp. 3925–3929.
- [129] B. Abdollahi, A. Soliman, A.C. Civelek, X.-F. Li, G. Gimel'farb, A. El-Baz, A novel Gaussian scale space-based joint MGRF framework for precise lung segmentation, in: *Proceedings of IEEE International Conference on Image Processing (ICIP'12)*, IEEE, 2012, pp. 2029–2032.

- [130] B. Abdollahi, A. Soliman, A.C. Civelek, X.-F. Li, G. Gimel'farb, A. El-Baz, A novel 3D joint MGRF framework for precise lung segmentation, in: *Machine Learning in Medical Imaging*, Springer, 2012, pp. 86–93.
- [131] A.M. Ali, A.S. El-Baz, A.A. Farag, A novel framework for accurate lung segmentation using graph cuts, in: *Proceedings of IEEE International Symposium on Biomedical Imaging: From Nano to Macro (ISBI'07)*, IEEE, 2007, pp. 908–911.
- [132] A. El-Baz, G.M. Beache, G. Gimel'farb, K. Suzuki, K. Okada, Lung Imaging Data Analysis, *Int. J. Biomed. Imaging* 2013 (2013) 1–2.
- [133] A. El-Baz, G.M. Beache, G. Gimel'farb, K. Suzuki, K. Okada, A. Elnakib, A. Soliman, B. Abdollahi, Computer-Aided Diagnosis Systems for Lung Cancer: Challenges and Methodologies, *Int. J. Biomed. Imaging* 2013 (2013) 1–46.
- [134] A. El-Baz, A. Elnakib, M. Abou El-Ghar, G. Gimel'farb, R. Falk, A. Farag, Automatic detection of 2D and 3D lung nodules in chest spiral CT scans, *Int. J. Biomed. Imaging* 2013 (2013) 1–11.
- [135] A. El-Baz, A.A. Farag, R. Falk, R. La Rocca, A unified approach for detection, visualization, and identification of lung abnormalities in chest spiral CT scans, in: *International Congress Series*, vol. 1256, Elsevier, 2003, pp. 998–1004.
- [136] A. El-Baz, A.A. Farag, R. Falk, R. La Rocca, Detection, visualization and identification of lung abnormalities in chest spiral CT scan: phase-I, in: *Proceedings of International Conference on Biomedical Engineering*, Cairo, Egypt, vol. 12, 2002.
- [137] A. El-Baz, A. Farag, G. Gimel'farb, R. Falk, M.A. El-Ghar, T. Eldiasty, A framework for automatic segmentation of lung nodules from low dose chest CT scans, in: *Proceedings of International Conference on Pattern Recognition (ICPR'06)*, vol. 3, IEEE, 2006, pp. 611–614.
- [138] A. El-Baz, A. Farag, G. Gimel'farb, R. Falk, M.A. El-Ghar, A novel level set-based computer-aided detection system for automatic detection of lung nodules in low dose chest computed tomography scans, *Lung Imaging Comput. Aided Diagn.* 10 (2011) 221–238.
- [139] A. El-Baz, G. Gimel'farb, M. Abou El-Ghar, R. Falk, Appearance-based diagnostic system for early assessment of malignant lung nodules, in: *Proceedings of IEEE International Conference on Image Processing (ICIP'12)*, IEEE, 2012, pp. 533–536.
- [140] A. El-Baz, G. Gimel'farb, R. Falk, A novel 3D framework for automatic lung segmentation from low dose CT images, in: A. El-Baz, J.S. Suri (Eds.), *Lung Imaging and Computer Aided Diagnosis*, Taylor & Francis, 2011, pp. 1–16, ISBN 978-1-4398-4558-5 (Chapter 1).
- [141] A. El-Baz, G. Gimel'farb, R. Falk, M. El-Ghar, Appearance analysis for diagnosing malignant lung nodules, in: *Proceedings of IEEE International Symposium on Biomedical Imaging: From Nano to Macro (ISBI'10)*, IEEE, 2010, pp. 193–196.
- [142] A. El-Baz, G. Gimel'farb, R. Falk, M.A. El-Ghar, A novel level set-based CAD system for automatic detection of lung nodules in low dose chest CT scans, in: A. El-Baz, J.S. Suri (Eds.), *Lung Imaging and Computer Aided Diagnosis*, vol. 1, Taylor & Francis, 2011, pp. 221–238, ISBN 978-1-4398-4558-5 (Chapter 10).
- [143] A. El-Baz, G. Gimel'farb, R. Falk, M.A. El-Ghar, A new approach for automatic analysis of 3D low dose CT images for accurate monitoring the detected lung nodules, in: *Proceedings of International Conference on Pattern Recognition (ICPR'08)*, IEEE, 2008, pp. 1–4.
- [144] A. El-Baz, G. Gimel'farb, R. Falk, M.A. El-Ghar, A novel approach for automatic follow-up of detected lung nodules, in: *Proceedings of IEEE International Conference on Image Processing (ICIP'07)*, vol. 5, IEEE, 2007, p. V-501.
- [145] A. El-Baz, G. Gimel'farb, R. Falk, M.A. El-Ghar, A new CAD system for early diagnosis of detected lung nodules, in: *IEEE International Conference on Image Processing*, 2007. *ICIP* 2007, vol. 2, IEEE, 2007, p. II-461.
- [146] A. El-Baz, G. Gimel'farb, R. Falk, M.A. El-Ghar, H. Refaie, Promising results for early diagnosis of lung cancer, in: *Proceedings of IEEE International Symposium on Biomedical Imaging: From Nano to Macro (ISBI'08)*, IEEE, 2008, pp. 1151–1154.

- [147] A. El-Baz, G.L. Gimel'farb, R. Falk, M. Abou El-Ghar, T. Holland, T. Shaffer, A new stochastic framework for accurate lung segmentation, in: *Proceedings of Medical Image Computing and Computer-Assisted Intervention (MICCAI'08)*, 2008, pp. 322–330.
- [148] A. El-Baz, G.L. Gimel'farb, R. Falk, D. Heredis, M. Abou El-Ghar, A novel approach for accurate estimation of the growth rate of the detected lung nodules, in: *Proceedings of International Workshop on Pulmonary Image Analysis*, 2008, pp. 33–42.
- [149] A. El-Baz, G.L. Gimel'farb, R. Falk, T. Holland, T. Shaffer, A framework for unsupervised segmentation of lung tissues from low dose computed tomography images, in: *Proceedings of British Machine Vision (BMVC'08)*, 2008, pp. 1–10.
- [150] A. El-Baz, G. Gimel'farb, R. Falk, M.A. El-Ghar, 3D MGRF-based appearance modeling for robust segmentation of pulmonary nodules in 3D LDCT chest images, in: *Lung Imaging and Computer Aided Diagnosis*, 2011, pp. 51–63 (Chapter 3).
- [151] A. El-Baz, G. Gimel'farb, R. Falk, M.A. El-Ghar, Automatic analysis of 3D low dose CT images for early diagnosis of lung cancer, *Pattern Recogn.* 42 (6) (2009) 1041–1051.
- [152] A. El-Baz, G. Gimel'farb, R. Falk, M.A. El-Ghar, S. Rainey, D. Heredia, T. Shaffer, Toward early diagnosis of lung cancer, in: *Proceedings of Medical Image Computing and Computer-Assisted Intervention (MICCAI'09)*, Springer, 2009, pp. 682–689.
- [153] A. El-Baz, G. Gimel'farb, R. Falk, M.A. El-Ghar, J. Suri, Appearance analysis for the early assessment of detected lung nodules, in: *Lung Imaging and Computer Aided Diagnosis*, CRC Press, Boca Raton, FL, 2011, pp. 395–404 (Chapter 17).
- [154] A. El-Baz, F. Khalifa, A. Elnakib, M. Nitzken, A. Soliman, P. McClure, G. Gimel'farb, M.A. El-Ghar, A novel approach for global lung registration using 3D Markov Gibbs appearance model, in: *Proceedings of International Conference Medical Image Computing and Computer-Assisted Intervention (MICCAI'12)*, Nice, France, October 1–5, 2012, pp. 114–121.
- [155] A. El-Baz, M. Nitzken, A. Elnakib, F. Khalifa, G. Gimel'farb, R. Falk, M.A. El-Ghar, 3D shape analysis for early diagnosis of malignant lung nodules, in: *Proceedings of International Conference Medical Image Computing and Computer-Assisted Intervention (MICCAI'11)*, Toronto, Canada, September 18–22, 2011, pp. 175–182.
- [156] A. El-Baz, M. Nitzken, G. Gimel'farb, E. Van Bogaert, R. Falk, M.A. El-Ghar, J. Suri, Three-dimensional shape analysis using spherical harmonics for early assessment of detected lung nodules, in: *Lung Imaging and Computer Aided Diagnosis*, CRC Press, Boca Raton, FL, 2011, pp. 421–438 (Chapter 19).
- [157] A. El-Baz, M. Nitzken, F. Khalifa, A. Elnakib, G. Gimel'farb, R. Falk, M.A. El-Ghar, 3D shape analysis for early diagnosis of malignant lung nodules, in: *Proceedings of International Conference on Information Processing in Medical Imaging (IPMI'11)*, Monastery Irsee, Germany (Bavaria), July 3–8, 2011, pp. 772–783.
- [158] A. El-Baz, M. Nitzken, E. Vanbogaert, G. Gimel'Farb, R. Falk, M. Abo El-Ghar, A novel shape-based diagnostic approach for early diagnosis of lung nodules, in: *2011 IEEE International Symposium on Biomedical Imaging: From Nano to Macro*, IEEE, 2011, pp. 137–140.
- [159] A. El-Baz, P. Sethu, G. Gimel'farb, F. Khalifa, A. Elnakib, R. Falk, M.A. El-Ghar, Elastic phantoms generated by microfluidics technology: validation of an imaged-based approach for accurate measurement of the growth rate of lung nodules, *Biotechnol. J.* 6 (2) (2011) 195–203.
- [160] A. El-Baz, P. Sethu, G. Gimel'farb, F. Khalifa, A. Elnakib, R. Falk, M.A. El-Ghar, A new validation approach for the growth rate measurement using elastic phantoms generated by state-of-the-art microfluidics technology, in: *Proceedings of IEEE International Conference on Image Processing (ICIP'10)*, Hong Kong, September 26–29, 2010, pp. 4381–4383.
- [161] A. El-Baz, P. Sethu, G. Gimel'farb, F. Khalifa, A. Elnakib, R. Falk, M.A. El-Ghar, J. Suri, Validation of a new imaged-based approach for the accurate estimating of the growth rate of detected lung nodules using real CT images and elastic phantoms generated by state-of-the-art microfluidics technology,

- in: A. El-Baz, J.S. Suri (Eds.), *Handbook of Lung Imaging and Computer Aided Diagnosis*, vol. 1, Taylor & Francis, New York, NY, 2011, pp. 405–420, ISBN 978-1-4398-4557-8 (Chapter 18).
- [162] A. El-Baz, A. Soliman, P. McClure, G. Gimel'farb, M.A. El-Ghar, R. Falk, Early assessment of malignant lung nodules based on the spatial analysis of detected lung nodules, in: *Proceedings of IEEE International Symposium on Biomedical Imaging: From Nano to Macro (ISBI'12)*, IEEE, 2012, pp. 1463–1466.
- [163] A. El-Baz, S.E. Yuksel, S. Elshazly, A.A. Farag, Non-rigid registration techniques for automatic follow-up of lung nodules, in: *Proceedings of Computer Assisted Radiology and Surgery (CARS'05)*, vol. 1281, Elsevier, 2005, pp. 1115–1120.
- [164] A.S. El-Baz, J.S. Suri, *Lung Imaging and Computer Aided Diagnosis*, CRC Press, Boca Raton, FL, 2011.
- [165] A. Soliman, F. Khalifa, N. Dunlap, B. Wang, M. El-Ghar, A. El-Baz, An ISO-surfaces based local deformation handling framework of lung tissues, in: *2016 IEEE 13th International Symposium on Biomedical Imaging (ISBI)*, IEEE, 2016, pp. 1253–1259.
- [166] A. Soliman, F. Khalifa, A. Shaffie, N. Dunlap, B. Wang, A. Elmaghraby, A. El-Baz, Detection of lung injury using 4D-CT chest images, in: *2016 IEEE 13th International Symposium on Biomedical Imaging (ISBI)*, IEEE, 2016, pp. 1274–1277.
- [167] A. Soliman, F. Khalifa, A. Shaffie, N. Dunlap, B. Wang, A. Elmaghraby, G. Gimel'farb, M. Ghazal, A. El-Baz, A comprehensive framework for early assessment of lung injury, in: *2017 IEEE International Conference on Image Processing (ICIP)*, IEEE, 2017, pp. 3275–3279.
- [168] A. Shaffie, A. Soliman, M. Ghazal, F. Taher, N. Dunlap, B. Wang, A. Elmaghraby, G. Gimel'farb, A. El-Baz, A new framework for incorporating appearance and shape features of lung nodules for precise diagnosis of lung cancer, in: *2017 IEEE International Conference on Image Processing (ICIP)*, IEEE, 2017, pp. 1372–1376.
- [169] A. Soliman, F. Khalifa, A. Shaffie, N. Liu, N. Dunlap, B. Wang, A. Elmaghraby, G. Gimel'farb, A. El-Baz, Image-based CAD system for accurate identification of lung injury, in: *2016 IEEE International Conference on Image Processing (ICIP)*, IEEE, 2016, pp. 121–125.
- [170] B. Dombroski, M. Nitzken, A. Elnakib, F. Khalifa, A. El-Baz, M.F. Casanova, Cortical surface complexity in a population-based normative sample, *Transl. Neurosci.* 5 (1) (2014) 17–24.
- [171] A. El-Baz, M. Casanova, G. Gimel'farb, M. Mott, A. Switala, An MRI-based diagnostic framework for early diagnosis of dyslexia, *Int. J. Comput. Assist. Radiol. Surg.* 3 (3–4) (2008) 181–189.
- [172] A. El-Baz, M. Casanova, G. Gimel'farb, M. Mott, A. Switala, E. Vanbogaert, R. McCracken, A new CAD system for early diagnosis of dyslexic brains, in: *Proceedings of the International Conference on Image Processing (ICIP'2008)*, IEEE, 2008, pp. 1820–1823.
- [173] A. El-Baz, M.F. Casanova, G. Gimel'farb, M. Mott, A.E. Switwala, A new image analysis approach for automatic classification of autistic brains, in: *Proceedings of the IEEE International Symposium on Biomedical Imaging: From Nano to Macro (ISBI'2007)*, IEEE, 2007, pp. 352–355.
- [174] A. El-Baz, A. Elnakib, F. Khalifa, M.A. El-Ghar, P. McClure, A. Soliman, G. Gimel'farb, Precise segmentation of 3-D magnetic resonance angiography, *IEEE Trans. Biomed. Eng.* 59 (7) (2012) 2019–2029.
- [175] A. El-Baz, A. Farag, G. Gimel'farb, M.A. El-Ghar, T. Eldiasty, Probabilistic modeling of blood vessels for segmenting MRA images, in: *18th International Conference on Pattern Recognition (ICPR'06)*, vol. 3, IEEE, 2006, pp. 917–920.
- [176] A. El-Baz, A.A. Farag, G. Gimel'farb, M.A. El-Ghar, T. Eldiasty, A new adaptive probabilistic model of blood vessels for segmenting MRA images, in: *Medical Image Computing and Computer-Assisted Intervention—MICCAI 2006*, vol. 4191, Springer, 2006, pp. 799–806.
- [177] A. El-Baz, A.A. Farag, G. Gimel'farb, S.G. Hushek, Automatic cerebrovascular segmentation by accurate probabilistic modeling of TOF-MRA images, in: *Medical Image Computing and Computer-Assisted Intervention—MICCAI 2005*, Springer, 2005, pp. 34–42.

- [178] A. El-Baz, A. Farag, A. Elnakib, M.F. Casanova, G. Gimel'farb, A.E. Switala, D. Jordan, S. Rainey, Accurate automated detection of autism related corpus callosum abnormalities, *J. Med. Syst.* 35 (5) (2011) 929–939.
- [179] A. El-Baz, A. Farag, G. Gimelfarb, Cerebrovascular segmentation by accurate probabilistic modeling of TOF-MRA images, in: *Image Analysis*, vol. 3540, Springer, 2005, pp. 1128–1137.
- [180] A. El-Baz, G. Gimel'farb, R. Falk, M.A. El-Ghar, V. Kumar, D. Heredia, A novel 3D joint Markov-Gibbs model for extracting blood vessels from PC-MRA images, in: *Medical Image Computing and Computer-Assisted Intervention—MICCAI 2009*, vol. 5762, Springer, 2009, pp. 943–950.
- [181] A. Elnakib, A. El-Baz, M.F. Casanova, G. Gimel'farb, A.E. Switala, Image-based detection of corpus callosum variability for more accurate discrimination between dyslexic and normal brains, in: *Proceedings of the IEEE International Symposium on Biomedical Imaging: From Nano to Macro (ISBI'2010)*, IEEE, 2010, pp. 109–112.
- [182] A. Elnakib, M.F. Casanova, G. Gimel'farb, A.E. Switala, A. El-Baz, Autism diagnostics by centerline-based shape analysis of the corpus callosum, in: *Proceedings of the IEEE International Symposium on Biomedical Imaging: From Nano to Macro (ISBI'2011)*, IEEE, 2011, pp. 1843–1846.
- [183] A. Elnakib, M. Nitzken, M.F. Casanova, H. Park, G. Gimel'farb, A. El-Baz, Quantification of age-related brain cortex change using 3D shape analysis, in: *2012 21st International Conference on Pattern Recognition (ICPR)*, IEEE, 2012, pp. 41–44.
- [184] M. Mostapha, A. Soliman, F. Khalifa, A. Elnakib, A. Alansary, M. Nitzken, M.F. Casanova, A. El-Baz, A statistical framework for the classification of infant DT images, in: *2014 IEEE International Conference on Image Processing (ICIP)*, IEEE, 2014, pp. 2222–2226.
- [185] M. Nitzken, M.F. Casanova, G. Gimel'farb, A. Elnakib, F. Khalifa, A. Switala, A. El-Baz, 3D shape analysis of the brain cortex with application to dyslexia, in: *2011 18th IEEE International Conference on Image Processing (ICIP)*, September, IEEE, Brussels, Belgium, 2011, pp. 2657–2660 (Selected for oral presentation. Oral acceptance rate is 10% and the overall acceptance rate is 35%).
- [186] E.E.-Z.A. El-Gamal, M.M. Elmogy, M. Ghazal, A. Atwan, G.N. Barnes, M.F. Casanova, R. Keynton, A. S. El-Baz, A novel CAD system for local and global early diagnosis of Alzheimer's disease based on PIB-PET scans, in: *2017 IEEE International Conference on Image Processing (ICIP)*, IEEE, 2017, pp. 3270–3274.
- [187] M. Ismail, A. Soliman, M. Ghazal, A.E. Switala, G. Gimel'farb, G.N. Barnes, A. Khalil, A. El-Baz, A fast stochastic framework for automatic MR brain images segmentation, *PLoS ONE* 12 (11) (2017) e0187391.
- [188] M.M.T. Ismail, R.S. Keynton, M.M.M.O. Mostapha, A.H. ElTanboly, M.F. Casanova, G.L. Gimel'farb, A. El-Baz, Studying autism spectrum disorder with structural and diffusion magnetic resonance imaging: a survey, *Front. Hum. Neurosci.* 10 (2016) 211.
- [189] A. Alansary, M. Ismail, A. Soliman, F. Khalifa, M. Nitzken, A. Elnakib, M. Mostapha, A. Black, K. Stinebruner, M.F. Casanova, et al., Infant brain extraction in T1-weighted MR images using BET and refinement using LCDG and MGRF models, *IEEE J. Biomed. Health Inform.* 20 (3) (2016) 925–935.
- [190] M. Ismail, A. Soliman, A. ElTanboly, A. Switala, M. Mahmoud, F. Khalifa, G. Gimel'farb, M. F. Casanova, R. Keynton, A. El-Baz, Detection of white matter abnormalities in MR brain images for diagnosis of autism in children, in: *2016 IEEE 13th International Symposium on Biomedical Imaging (ISBI)*, IEEE, 2016, pp. 6–9.
- [191] M. Ismail, M. Mostapha, A. Soliman, M. Nitzken, F. Khalifa, A. Elnakib, G. Gimel'farb, M.F. Casanova, A. El-Baz, Segmentation of infant brain MR images based on adaptive shape prior and higher-order MGRF, in: *2015 IEEE International Conference on Image Processing (ICIP)*, IEEE, 2015, pp. 4327–4331.
- [192] E.H. Asl, M. Ghazal, A. Mahmoud, A. Aslantas, A. Shalaby, M. Casanova, G. Barnes, G. Gimel'farb, R. Keynton, A. El-Baz, Alzheimer's disease diagnostics by a 3D deeply supervised adaptable convolutional network, *Front. Biosci. (Landmark Ed.)* 23 (2018) 584–596.

- [193] A. Mahmoud, A. El-Barkouky, H. Farag, J. Graham, A. Farag, A non-invasive method for measuring blood flow rate in superficial veins from a single thermal image, in: *Proceedings of the IEEE Conference on Computer Vision and Pattern Recognition Workshops*, 2013, pp. 354–359.
- [194] A. El-Baz, A. Shalaby, F. Taher, M. El-Baz, M. Ghazal, M.A. El-Ghar, A.L.I. Takieldeem, J. Suri, Probabilistic modeling of blood vessels for segmenting magnetic resonance angiography images, *Med. Res. Arch.* 5 (3) (2017) 1–22.
- [195] A.S. Chowdhury, A.K. Rudra, M. Sen, A. Elnakib, A. El-Baz, Cerebral white matter segmentation from MRI using probabilistic graph cuts and geometric shape priors, in: *ICIP*, 2010, pp. 3649–3652.
- [196] Y. Gebru, G. Giridharan, M. Ghazal, A. Mahmoud, A. Shalaby, A. El-Baz, Detection of cerebrovascular changes using magnetic resonance angiography, in: *Cardiovascular Imaging and Image Analysis*, CRC Press, Boca Raton, FL, 2018, pp. 1–22.
- [197] A. Mahmoud, A. Shalaby, F. Taher, M. El-Baz, J.S. Suri, A. El-Baz, Vascular tree segmentation from different image modalities, in: *Cardiovascular Imaging and Image Analysis*, CRC Press, Boca Raton, FL, 2018, pp. 43–70.
- [198] F. Taher, A. Mahmoud, A. Shalaby, A. El-Baz, A review on the cerebrovascular segmentation methods, in: *2018 IEEE International Symposium on Signal Processing and Information Technology (ISSPIT)*, IEEE, 2018, pp. 359–364.
- [199] H. Kandil, A. Soliman, L. Fraiwan, A. Shalaby, A. Mahmoud, A. ElTanboly, A. Elmaghraby, G. Giridharan, A. El-Baz, A novel MRA framework based on integrated global and local analysis for accurate segmentation of the cerebral vascular system, in: *2018 IEEE 15th International Symposium on Biomedical Imaging (ISBI 2018)*, IEEE, 2018, pp. 1365–1368.